NAIST-IS-DD1161204

Doctoral Dissertation

Axial Optical Tweezers for the Measurement of Localized Cell Stiffness

Mary-Clare Clarin Dy

September 25, 2013

Department of Bioinformatics and Genomics
Graduate School of Information Science
Nara Institute of Science and Technology

A Doctoral Dissertation
submitted to Graduate School of Information Science,
Nara Institute of Science and Technology
in partial fulfillment of the requirements for the degree of
Doctor of ENGINEERING

Mary-Clare Clarin Dy

Thesis Committee:

Professor Shigehiko KANAYA	(Supervisor)
Professor Tsukasa OGASAWARA	(Co-supervisor)
Associate Professor Tadao SUGIURA	(Co-supervisor)

Axial Optical Tweezers for the Measurement of Localized Cell Stiffness*

Mary-Clare Clarin Dy

Abstract

Designing an optical tweezers to apply constant force on the cell and computing the cell stiffness can offer insights about how cells respond to outside mechanical stimulus [1], which in turn can provide vital information about cellular functions such as cell motility and mitosis of cancer cells [2].

Cells and biomolecules are typically investigated using lateral manipulation of the optical tweezers. Because cells move in three dimensions, incorporating an axial mechanical stimulus can elucidate the overall effect of forces exerted on biological materials. Studies that investigate axial manipulation integrate other devices such as spatial light modulators, and deformable mirrors, or modify the laser pattern, yet these studies concentrate on measuring three-dimensional particle position, trapping stiffness, and forces.

To integrate an axial manipulation system but, at the same time, minimize the modification of existing optical tweezers setups, a simple scheme is proposed: an optical trap system is designed to manipulate particles in the axial direction using motorized lens. The particle movement with nanometer sensitivity is estimated using image analysis techniques. 4 μm- and 2 μm-sized polystyrene particles are axially manipulated for approximately 5 μm and 6 μm, respectively. The system is applied on the measurement of localized cell stiffness using the equation of Hertz model. A series of experiments are performed to obtain the necessary parameters for the localized cell stiffness computation. The trapping stiffness,

*Doctoral Dissertation, Department of Bioinformatics and Genomics, Graduate School of Information Science, Nara Institute of Science and Technology, NAIST-IS-DD1161204, September 25, 2013.

the forces exerted on a Balb3T3 cell, and the cell deformation are evaluated. The localized cell stiffness computations for a given cell sample are 17 Pa and 40 Pa using 4 μm- and 2 μm-sized particles, respectively. Results suggest that the proposed optical tweezers scheme can obtain the necessary parameters for the computation of localized cell stiffness using Hertz model equation.

Keywords:

Optical tweezers, Axial particle manipulation, Image processing, Cell stiffness measurement, Hertz model

Contents

List of Figures

List of Tables

Chapter 1

Introduction

This chapter sets the theme of the dissertation: Section 1.1 discusses the importance of studying the mechanical properties of cells, and how optical tweezers plays an important role in the field of bio- and nanotechnology. Section 1.2 to 1.4 introduce the problems that led to the development of the axial movement of optical tweezers and the proposed solution for the measurement of localized cell stiffness. Finally, Section 1.5 provides an outline for the succeeding chapters.

1.1 Research Motivation

The molecular functions and structures of cells are studied based on the biological and chemical reactions of the different proteins, deoxyribonucleic acid (DNA), ribonucleic acid (RNA), lipids, and other cellular components. Due to advancing nanotechnology, new tools and methods have emerged for the development of biotechnology. [11]. The mechanical studies on the cytoskeleton can provide important information into the function of biological molecules such as cell division, motility, mobility, growth of neuron cells, and study of adaptive immune system [2,12]. Going further into the cell structure: the cytoskeletal components, such as actin filaments and microtubules, can be mechanically stimulated and have been shown to play crucial roles in mediating and transferring sub-cellular local signals to the whole cell [13]. Fig. 1.1 shows some applications where measuring the mechanical properties of cells have significant contributions.

In Fig. 1.1(a), González-Cruz proposed that the mechanical characteristics of

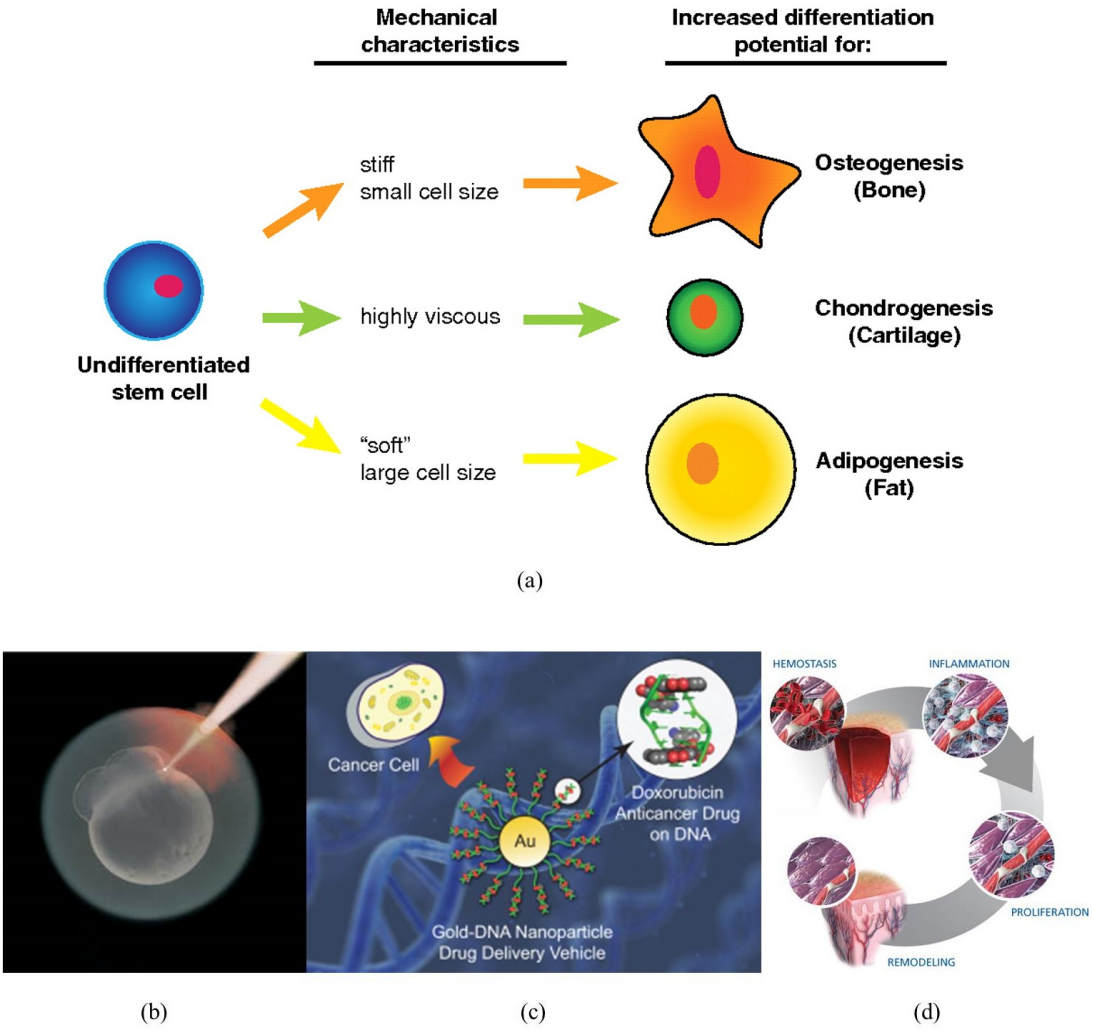

Figure 1.1: Biomedical applications involving the measurement of mechanical properties of cells. (a) Different measures of mechanical properties can help predict the outcome of undifferentiated stem cells [3]. (b) Knowledge of viscosity and elasticity are necessary for laser surgery on the cellular level (http://www.photonicsonline.com). (c) Cancer research and improved drug delivery (http://oncozine.com). (d) Cell elasticity changes for different stages of wound healing in tissue engineering (http://www.cytomedix.com).

undifferentiated stem cells indicate the cell potential. The investigated relationship can be utilized as an alternative means of identifying lineage-specific adipose tissue stem cells for cell-based therapies. The elastic and viscoelastic parameters showed significant correlations with the aforementioned stem cell mechanical biomarkers and the production of lineage-specific molecules that characterize the differentiated cell types. It showed that stiff cells that have small sizes are likely to become osteogenic, having positive correlation with elastic moduli. On the other hand, highly viscous cells have greater chondrogenic potential as indicated by the positive correlation with apparent viscosity. Finally, large, yet soft cells may become adipocytes because of positive correlation with size, and negative correlation with elastic moduli [3]. van de Stolpe reported that blood circulating tumor cell (CTC) enumeration and molecular characterization increasingly provide clinical information on prognosis, therapy choice, and drug resistance and effectiveness. Different techniques such as filtering, dielectrophoresis, and EpiSpot technology are used to distinguish the size and mechanical properties of CTCs from normal blood cells [14]. Being able to measure the mechanical properties of cells and the interacting forces, in collaboration with chemical and biological studies, can elucidate on the different roles of individual biomolecules. Investigation of cell stiffness may be applied in studies about tissue engineering, medical diagnostics, and cancer research, as shown in Fig. 1.1(b-c) [15–21].

Single-beam gradient trap, or optical tweezers, allows non-contact trapping and manipulation of microscopic particles including living cells and organelles within cells. It has been utilized to exert forces in the pN-order, which is suitable for studying the interacting forces between and within biomolecules [22, 23], the kinetics and properties of biological molecules [24], and measurements of forces acting on particles in colloidal suspensions [25,26]. Notable biological applications include stretching DNA, a red blood cell (RBC) [27], probing different types of cells to study focal adhesion [7,28], and tether formations [29]. Some experiments using three dimensional optical traps include manipulating sperm cells and measuring their swimming forces [30], microfluidic sorting, which demonstrates the sorting of protein microcapsule drug delivery agents by size, and sorting other colloidal particle streams by refractive index [31], and particle tracking using forward scattered light in the diffusion of glycosylphosphatidylinositol (GPI)-

anchored membrane protein on a neurite [32]. Several reviews have exhaustive literature and discussion about other applications of optical tweezers in biology and other fields [33–36].

1.2 Overview of the problem

There are three main problems that this dissertation will address. First, optical traps are typically designed to manipulate objects in the lateral direction [27, 37, 38]. This include, but not limited to, stretching RBCs and DNAs, and probing different cell types. To obtain a holistic view on the mechanical properties of cells, the study on the effects of axial forces is necessary. Other works that study axial position utilize special devices, such as acousto-optic modulators and spatial light modulators [39, 40]. Other works modify the laser beam pattern and utilize other imaging tools to detect particle movement in three dimensions [32, 41]. Integrating these devices in the existing optical tweezers setup is possible, but this will lead to the second problem: additional devices complicate the setup; not only will the control of the lateral manipulation of the optical trap may be compromised, more importantly, the third problem is that the axial cell stiffness is not measured even when these devices were utilized. Cell stiffness is primarily related to the cytoskeleton, which can reveal insights about the cell structure and physiology.

1.3 Research contribution

The main contributions of the dissertation is the design of an axial manipulation system using optical tweezers, and its application in the measurement of localized cell stiffness. The proposed approach can manipulate particles in the axial direction by controlling the position of one optical component. This design eliminates the necessity of integrating other devices in the existing setup. The scheme can measure the corresponding particle position within the nanometer range. Being able to measure small particle movements is needed especially for measuring the trapping stiffness, and estimating the deformations made on a cell. Finally, the proposed system is used to obtain the necessary parameters for the measurement

of the localized cell stiffness, following the Hertz model equation.

1.4 Research tasks and limitations

The work presented in this dissertation is conducted in separate experiments. To clarify the flow of the dissertation, the experiments are described in series, yet the actual experiments can be done in any order. The first task is to develop the program that move the optical trap along the optical axis. The program also includes the command for the charged-coupled device (CCD) camera to take images of the manipulated particle. A separate program is also developed for image analysis. The second task is to move particles in the axial direction for a given length. This experiment reveal the default position and useful length of axial particle movement. Third task is the trapping stiffness experiment, wherein the fluctuations of a trapped particle are observed. The cell experiment is conducted as the fourth task. Using the default position and determined length of axial particle movement, a particle is set on the cell surface, and the cell is probed using downward and upward motions. Task 1 provides the means to estimate particle movement while Tasks 2 to 4 provide the results that is used to evaluate all the parameters necessary for the computation of task 5, which is to measure the localized cell stiffness using Hertz model equation.

The localized cell stiffness is emphasized because the dissertation does not evaluate the elastic modulus of the whole cell. Rather, the cell is probed using the small force exerted by the optical trap. Also, the cellular components activated during the cell adhesion and deformation are not identified.

1.5 Dissertation layout

The dissertation is organized as follows:

This chapter introduced the role and importance of nanomanipulation in biological applications. The research contributions and the dissertation layout were also given in this chapter. **Chapter Two** gives the overview of related works. A brief discussion about atomic force microscopy will be tackled as a comparison with optical tweezers. The theory of how optical tweezers is manipulated

in the axial direction will be emphasized. The equipartition theorem, Hooke's Law and Hertz model will also be explained. **Chapter Three** presents the axial optical tweezers setup and methodology. The image processing and position analysis will be discussed in detail. **Chapter Four** covers the cell stiffness measurement. Measurement of force and trapping stiffness will be included in this chapter. Finally, **Chapter Five** concludes the dissertation.

Chapter 2

Related Literature

The previous chapter introduced the important contributions of measuring the cell stiffness in the biomedical field. The role of optical tweezers in measuring the mechanical properties of cells was also mentioned. The proposed system and its application were also briefly discussed. In this chapter, relevant research works and methodologies to be used are presented. Section 2.1 further explains two studies that deal mainly with forces and mechanical properties of cells. Section 2.2 opens the discussion of different nanomanipulation techniques. Two methods, atomic force microscopy (AFM) and optical tweezers, in particular, will be expounded. This section also includes the discussion of Cell Palpation System, which is the springboard of this dissertation topic. Section 2.3 provides detailed information about axial manipulation of optical tweezers. Sections 2.4 and 2.5 discuss how the trapping stiffness and force, and cell stiffness are measured, respectively. Finally, Section 2.6 provides a summary of the chapter.

2.1 Cell mechanics and single-molecule force spectroscopy

Force is an important factor that affects cells. One of the studies of the physical aspect of cells and other biological materials encompass the reactions of these materials to outside forces [42]. In relation to that, cell mechanics also aims to describe the mechanical properties of cells and cellular structures. It also eval-

uates the mechanical interactions between cells and their environment, wherein these living and changing entities (the cells) can alter their mechanical properties in response to external stimuli or force [1]. In effect, all biological motions are driven by molecular forces. Even the elimination and reduction of motion through ligand-receptor bindings or other formation of bonds have to overcome thermal and other forces. In this wide range of studies, single-molecule force spectroscopy has emerged as a powerful tool that can investigate the forces and motions associated with biological molecules and enzymatic activity [6].

In cell mechanics, different cellular structures have been proposed as sensors for the applied forces. These force sensor structures include, but are not limited to, the extracellular matrix (ECM), cytoskeleton, transmembrane proteins, and lipid bilayers. The measured elastic moduli that describe both the cells and global deformation in response to the forces, and the deformation of specific structures at the cell surface can help discriminate between different modes of mechanosensing. Fig. 2.1 shows the different structures in an animal cell and the ECM. The cytoskeleton and ECM are considered for their roles in mediating mechanical signals, and how they affect mechanically activated ion channels.

One model of mechanotransduction hypothesize that the cytoskeleton plays a central role in regulating membrane ion channels. It is proposed that cells regulate ion channel conductance, in part, by force transmission through adhesions to the cytoskeleton, and subsequent cytoskeletal modification of the gating properties of the channels [43]. As ion transport in various tissues can apparently be regulated by adhesion systems that interact with the cortical actin cytoskeleton, it has been suggested that stretch-sensitive channels may be able to sense mechanical signals delivered from the sub-membrane, cytoplasmic face of the cell, possibly involving physical linkages to the cytoskeleton [44].

Extracellular matrix is a conductor of mechanical forces but its structure and composition are also influenced by the cellular responses to those same applied or endogenously generated forces. Because of the unique surrounding protein matrices, cells likely sense and respond to applied forces differently. ECM plays a crucial role in cell adhesion, where focal adhesion or focal complexes are candidate sites for transfer of contractile forces to the cytoskeleton in both cultured cells and cells in tissues [13]. Attachment of connective tissue cells to the ECM is contingent

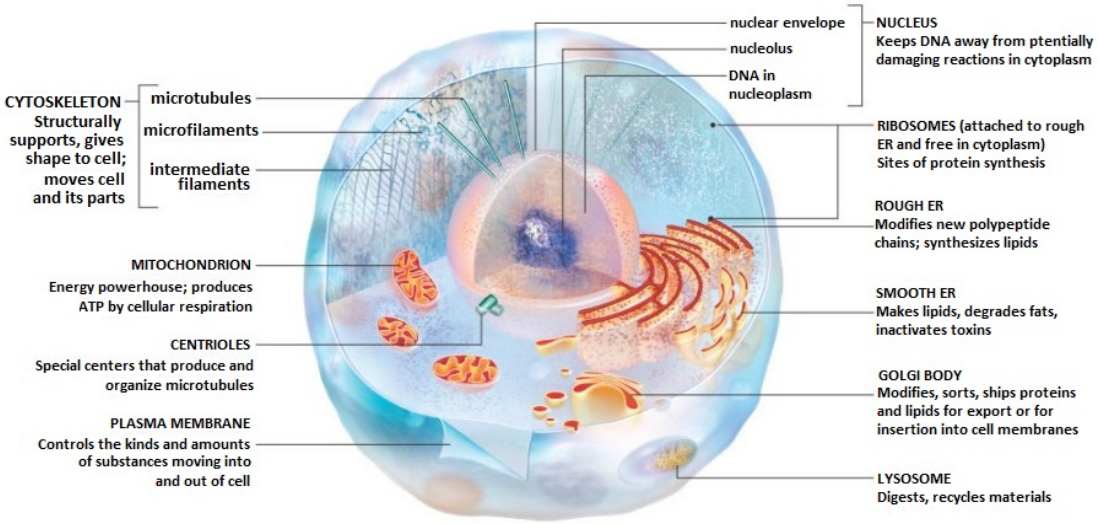

(a) Diagram of animal cell (www.yellowtang.org).

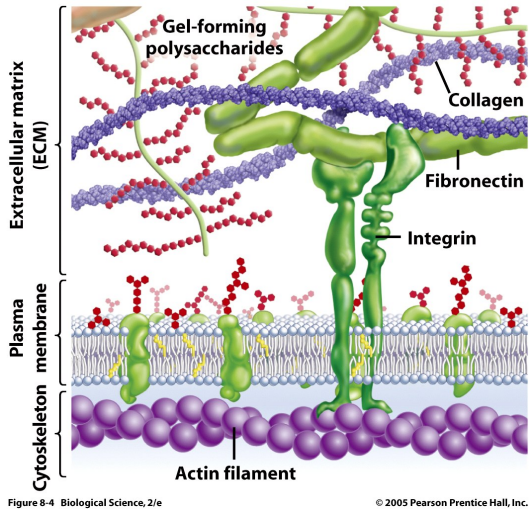

(b) Extracellular matrix (Pearson Prentice Hall, Inc.).

Figure 2.1: Different structures of cells such as the (a) cytoskeleton, proteins and lipid bilayers, and (b) extracellular matrix molecules have been considered as force sensors.

on the formation and remodeling of integrin-mediated adhesions, but cells also adhere to each other by intercellular adhesive molecules, such as cadherins, that may also act as force sensors [45].

For single-molecule force spectroscopy, earlier applications include the characterization of conventional motor protein such as kinesins and myosins [46–48]. The application of force provides a way to selectively modify the steps in a biochemical reaction cycle that involves motion. Detailed measurement of the force-extension relationship (elasticity) of individual polymers, in particular of nucleic acids [49, 50], opened up the possibility of investigating unconventional nucleic-acid molecular motors that translocate or otherwise modify DNA or RNA. Currently, single-molecule manipulation capacity spans six orders of magnitude in length (10^{-10} - 10^{-4} m) and force (10^{-14} - 10^{-8} N). Applications range from the manipulation of cells (approximately 100 μm) to the measurement of RNA polymerase advancing a single base pair (0.34 nm) along DNA [51], and from the mechanical disruption of covalent bonds in the order of nano-Newton forces [52] to assaying nucleic acid folding kinetics, which is approximately 0.1 pN [53].

2.2 Nanomanipulation in biological applications

Using nanomanipulation in the study of cell mechanics and force spectroscopy encompasses a wide area of investigation of essential cellular processes. Although the two areas of study are very much related, cell mechanics deal with how biological entities react to outside forces and transduce these mechanical signals into a cascade of biochemical signals that ultimately leads to a host of biological responses. On the other hand, force spectroscopy, in a general sense, concerns the application of force and measurement of displacement at the single-molecule level.

There are many techniques available for studying cell mechanics and single-molecule force spectroscopy, as shown in Fig. 2.2. Glass microneedles, cell pokers, and AFM can be utilized to apply mechanical indentation onto the cell surface [54–56]. On the other hand, micropipettes are used to apply mechanical tension to the cell membrane, especially to RBCs [57]. Shearing and compression between microplates, optical traps, and magnetic methods are other examples

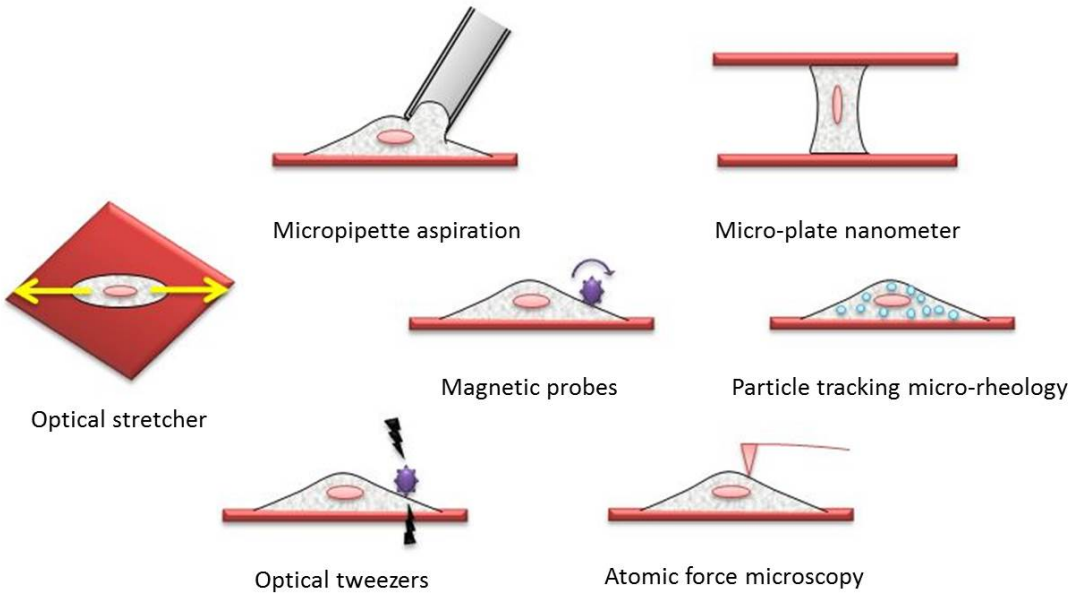

Figure 2.2: Examples of nanomanipulation techniques that measure the mechanical properties of cells (http://www.intechopen.com).

as well [33, 58, 59]. Table 2.1 shows different techniques used to measure the elastic modulus for cell mechanics [43]. Table 2.2 compares the three most commonly used single-molecule force spectroscopy techniques [6]. In the following subsections, two methods that are used in both studies are discussed. Atomic force microscopy (AFM) and optical tweezers are commonly utilized in studying biological entities, although these two methods are also applied in the study of inorganic materials. AFM has been utilized in quantifying surface forces, in directly measuring force law in liquids and vapors at angstrom resolution level, and calculating the forces necessary for bonding and bond breaking of, but not limited to, single polymer molecules [60–62]. In the case of optical tweezers, studies have been done on trapping metallic particles such as gold, aligning dielectric particles in aqueous environments, and measuring colloidal particle interactions [63–65].

Table 2.1: Comparison of elastic moduli measured for single cells in culture

Cell type	Elastic modulus (kPa)	Method	Reference
Rat aortic smooth muscle	1.5 - 11	Elongation between plates	[66]
Fibroblast	0.6 - 1.6	AFM	[67]
Fibroblast	1 - 10 (differential stretch modulus)	Uniaxial stretching/compression	[68]
Bovine articular chondrocytes	1.1 - 8	Creep cyoindentation apparatus	[69]
Chondrocytes, Endothelial	0.5	Microaspiration	[57]
Neutrophils passive/activated	0.38/0.8	AFM	[70]
C2C12 myoblasts	2	Cell loading device (global compression)	[71]
Alveolar epithelial	0.1 - 0.2	Magnetic twisting cytometry	[72]
Fibroblasts Normal/transformed	0.22/0.19; 0.42 - 0.48/1.0	Optical stretcher	[73, 74]
3T3 fibroblast before/after shear flow	0.015/0.06	Tracer diffusion	[75]
C2 - 7 myogenic	0.66	Uniaxial stretching rheometer	[76]

Table 2.2: Comparison of single-molecule force spectroscopy techniques

	Optical tweezers	(Electro) Magnetic tweezers	Atomic force microscopy
Spatial resolution (nm)	0.1 - 2	(2 - 10) 5 - 10	0.5 - 1
Temporal resolution (s)	10^{-4}	(10^{-4}) 10^{-1} - 10^{-2}	10^{-3}
Stiffness (pN nm^{-1})	0.005 - 1	(10^{-4}) 10^{-3} - 10^{-6}	10 - 10^{5}
Force range (pN)	0.1 - 100	(0.01 - 10^{4}) 10^{-3} - 10^{2}	10 - 10^{4}
Displacement range (nm)	0.1 - 10^{5}	(5 - 10^{5}) 5 - 10^{4} - 10^{-2}	0.5 - 10^{4}
Probe size (μm)	0.25 - 5	0.5 - 5	0100 - 250
Typical applications	3D manipulation Tethered assay Interaction assay	(3D manipulation) Topology Tethered assay DNA	High-force pulling Interaction assays
Features	Low-noise and low-drift dumbbell geometry	Force clamp Bead rotation Specific interactions	High-resolution imaging
Limitations	Photodamage Sample heating Nonspecific	(Force hysteresis) No manipulation	Large high-stiffness probe Large minimal force Nonspecific

2.2.1 Atomic Force Microscopy

Atomic force microscopy (AFM) is a part of the scanning probe microscope systems that can image surface topography of both insulating and conductive samples [77, 78]. The scanning principle of AFM will not be expounded in this dissertation, rather the focus will be on the principle on how AFM is able to apply and measure forces with high sensitivity, to position a tip relative to the sample in three dimensions with high precision, and to operate in liquids, thus making AFM viable for biological applications [56].

Fig. 2.3(a) shows a typical setup of AFM. A cantilever with sharp tip (yellow) is held above a piezoelectric stage (gray). The piezoelectric stage can move the sample relative to the tip with sub-nanometer displacement in three dimensions when a voltage is applied [78]. When the cantilever is deflected, a low power laser (red beam) is displaced. The position-sensitive detector (PSD) measures the laser beam displacement, thus effectively measuring the cantilever deflection. In this image, the AFM performs a pulling experiment. First, a molecule (purple) is attached to the sample surface (copper) and the cantilever tip. A piezoelectric stage is pulled down along the axial direction, increasing the distance between the cantilever and the sample surface. The force exerted on the molecule is computed from the cantilever deflection, while the extension of the molecule is the separation distance between the AFM tip and the sample surface [6]. Fig. 2.3(b) shows a different type of experiment, wherein cell deformation is created. In Puttini paper [4], tendons of muscle sections are attached to a glass coverslip. The sample is then placed in a "liquid cell" filled with medium. In Fig. 2.3(c), the differences in force curves of stiff (glass) and soft (muscle) samples are shown. To compute the force, cantilever behaves like linear springs for small deflections thus Hooke's law can be applied:

$$F = k_c \times (d - d_0), \tag{2.1}$$

where k_c is the force constant of the cantilever, d is the deflection or displacement of the cantilever, and F is the loading force exerted by the cantilever. The d_0 is the offset deflection caused by stresses in the cantilever even when no load is exerted on the cantilever [56].

These curves in Fig. 2.3(c) only reflect the duration when the cantilever tip is

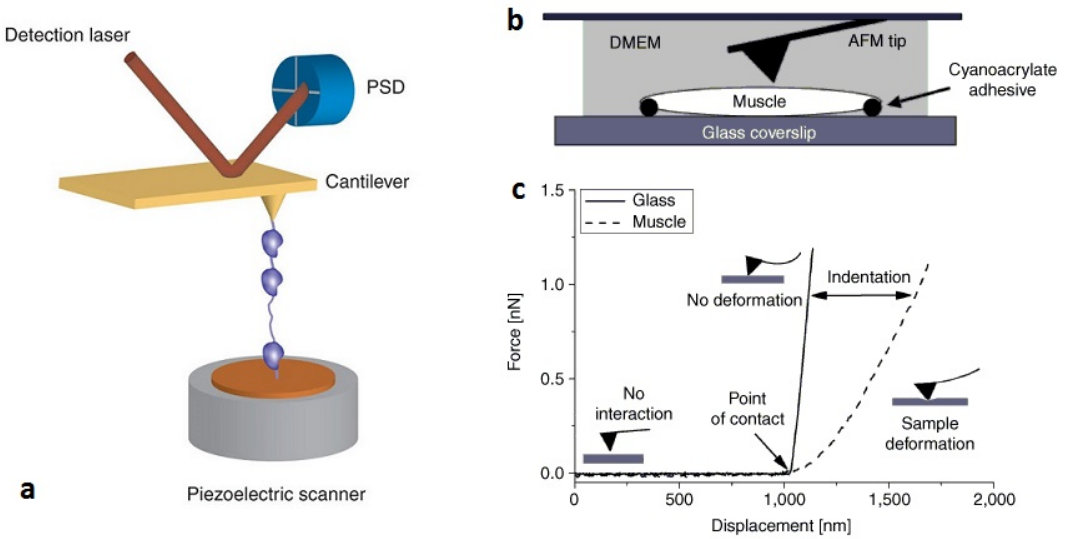

Figure 2.3: Atomic force microscopy. (a) Diagram of AFM pulling a molecule [6]. (b) Scheme of the experimental AFM setup and (c) Principles of the quantification of muscle elastic properties [4].

approaching the muscle surface. The force acting between the end of the tip and the investigated surface causes cantilever deflection. By monitoring this deflection as a function of relative sample position, the force applied versus the relative distance between the probe tip and the investigated surface can be recorded. The force curve of the glass shows negligible deformation as oppose to the force curve of the muscle sample. Subtracting the two curves results in the force-versus-indentation dependence that determines the elastic constant of the muscle sample [4].

From these sample experiments, the mechanical properties of cells, specifically the elastic constant, can be measured. Using force-curves, and the indentation measured, *Hertz model* can describe the elastic indentation of an infinitely extended sample by an indenter of simple shape [79]. The Hertz model will be expounded in Section 2.5.

2.2.2 Optical tweezers

Using a weakly focused laser beam, Arthur Ashkin first demonstrated the existence of gradient force that pulls particles with high refractive index towards the beam axis [80]. From this work, the foundation for optical trapping was set.

Single-beam gradient force optical traps or more commonly called as optical tweezers is created using a highly focused laser beam. Typically, the laser beam passes through an objective lens with high numerical aperture (NA). The focused laser beam converges to a narrow point called beam waist, which contains strong electric field gradient. When dielectric particles are introduced, these particles are attracted to the area with the strongest electric field, and are "pushed" by the laser light to travel in the direction of the beam propagation. Ashkin also observed that particles can be stably trapped and moved in three dimensions [5]. In order to create the stable trap, the gradient force must overcome the scattering forces that push the particle along the beam propagation, thus necessitating the very steep gradient obtained using the objective lens with high NA.

If the object is larger than the wavelength of the laser, ray optics diagram can explain the phenomenon of the optical trapping. Fig. 2.4(a) shows the ray optics diagram that describes the action of optical trap on a dielectric particle, in terms of total force originating from rays a and b, under the simplifying assumption of zero surface reflection. The dashed lines show the original focus position of the rays. The two forces, $\mathbf{F_a}$ and $\mathbf{F_b}$ are caused by refraction of the rays and are pointed towards the momentum change. A net restoring force $\mathbf{F_{total}}$ is directed towards the original focus position of the rays, thereby creating a stable trap [81]. The ray optics diagram that shows the action of the optical trap when the particle is displaced axially from the original focus is explained in Section 2.3. Fig. 2.4(b-c) show some applications of optical tweezers [6]. In Fig. 2.4(b), the optical tweezers (pink) is used to trap and manipulated a particle (green) coated with kinesin molecules (yellow). The trapped particle is manipulated towards the microtubule (brown), which is attached to a glass sample dish. The force and displacement of the individual kinesin molecule as it interacts with the microtubule can be measured from the displacement of the particle [82]. In Fig. 2.4(c), an RNA polymerase molecule (purple) is attached to a particle, while the free end of a DNA template is attached to a sample dish. As the DNA is transcribed,

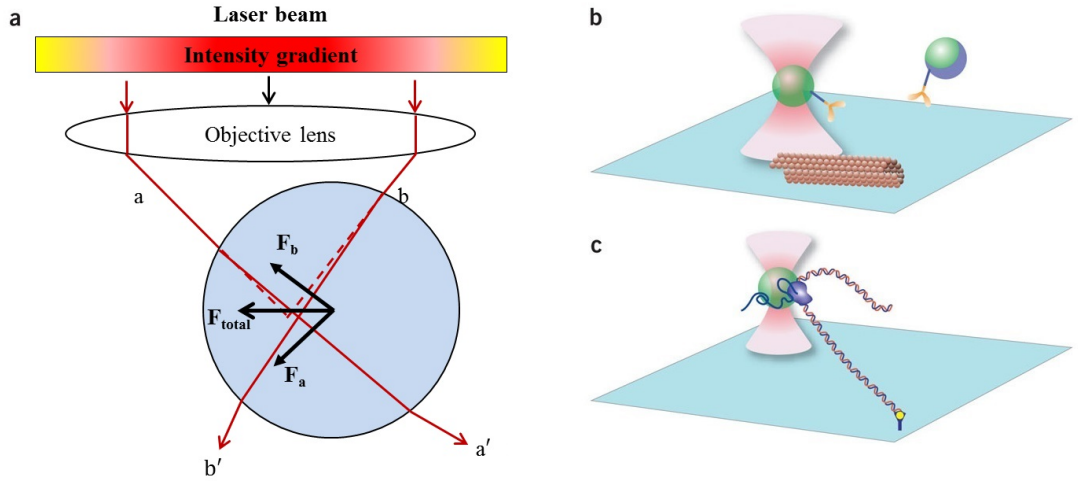

Figure 2.4: Optical tweezers. (a) Ray optics diagram depicting how optical tweezers maintain equilibrium when the particle is displaced laterally from the laser focus [5]. Some optical trap applications include (b) interaction assay: trapping and manipulating a particle to interact with other materials and (c) tethered assay [6]

the particle is pulled along the DNA by the polymerase. From this setup, the particle can be manipulated by the optical trap at constant force so that a long transcriptional record can be obtained [83]. Other optical tweezers applications include three-dimensional particle tracking [84, 85] and laser ablation or surgery, where in addition to using a continuous wave laser to trap and manipulate a particle, a pulsed laser ablates the cell sample that holds the particle [86, 87]. In particular, this work is based on one application which measures membrane support stiffness. The Cell Palpation System will be discussed in the following subsection.

2.2.3 Cell Palpation System

The mechanical properties of cell adhesion is measured with high sensitivity using an optically trapped particle. The Cell Palpation System (CPS) utilizes a particle as probe to apply mechanical stimulus to a cell and measure the reactive force. The particle was moved back-and-forth in a sinusoidal manner by changing the angle of galvano-mirror. This enabled the system to apply force and deform a

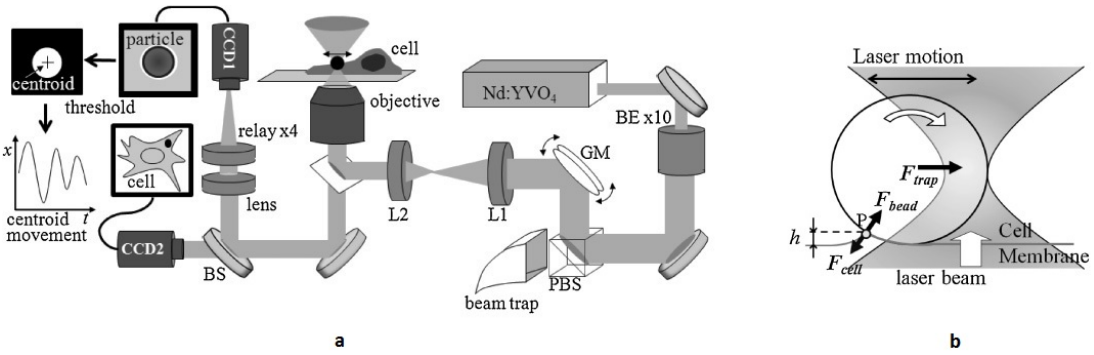

Figure 2.5: Cell Palpation System (a) Schematic diagram of CPS setup (b) Particle model manipulated by optical tweezers and attached to cell membrane [7].

cell sample. Fig. 2.5(a) shows the experimental setup of CPS. At the point of cell adhesion, which happens within a minute when the particle is attached on the cell, the schematic diagram of particle movement is shown in Fig.2.5(b).

When an attached particle is forced to move by the optical tweezers with force $\mathbf{F_{trap}}$, the particle was observed to roll on the membrane. Then the cell membrane was pulled up together with the particle at adhesion position P by the force of the particle rotation $\mathbf{F_{bead}}$. The reaction force $\mathbf{F_{cell}}$ was assumed to be proportional to the pulled height h of the cell membrane and provided information of the mechanical property of the cell adhesion. The motion equation of the particle is described as:

$$m\frac{d^2x}{dt^2} + 6\pi\eta_{med}r\frac{dx}{dt} + r\eta_{cell}\frac{dx}{dt} + \frac{1}{2r^2}Y(x+X_0)^3 = k[a\sin(\omega t) - x], \qquad (2.2)$$

where k is the spring constant of the optical tweezers, a is the amplitude of laser beam spot movement, ω is the angular velocity of the particle motion, x is the displacement of the particle center, m is the particle weight, η_{med} is the viscosity of surrounding medium, r is the particle radius, η_{cell} is the coefficient of viscosity of the cell membrane at position P, Y is the proportional constant of the response against membrane stiffness and X_0 is the displacement of particle migration caused by the fluidity of the cell membrane. The right part of the motion equation is the force applied to the particle from the optical tweezers. The Y, η_{cell}, and X_0 were estimated using Runge-Kutta method, and were determined

using least mean square method. The Y was defined as the membrane support stiffness because the parameter represents a property-like membrane stiffness supported by the membrane protein attached on the particle surface. The trapping stiffness was determined prior the experiment. Fig. 2.6 shows the results of experiments. Fig. 2.6(a) shows the motion of the laser beam spot and unattached particle, while Fig. 2.6(b) shows the laser beam spot and attached particle. It can be seen at Fig. 2.6(b) that the particle movement is attenuated, as oppose to Fig. 2.6(a) where the particle movement is synchronized with the laser beam spot. Fig. 2.6(c) shows an image of the cell and the positions A and B where particles were attached. Fig. 2.6(d) shows the computed membrane support stiffness of the cell at the respective positions. The difference in stiffness suggested that the components and characteristics of the cell membrane and/or membrane protein varies at measurement position. This phenomenon may have been affected by the increase in collage-integrin binding sites and/or reinforcement of the adhesion affected by the recruitment of cell adhesion-related molecules [88].

CPS have also been used to study the different particle coating for attaching certain protein in the cell membrane, and about endocytosis [89]. However, the optical trap is moved in lateral position. In order to study the effects of outside forces exerted from three dimensions, this dissertation focuses on developing an axial manipulation scheme.

2.3 Axial optical tweezers

Fig. 2.7 shows a ray-optics diagram that describes the scattering and optical momentum transfer to the particle. The diagram also explains how the laser beam is able to stably trap a particle in the axial direction [5, 80]. Without the presence of a particle, the rays a and b converges to a point, the laser focus. When a particle is introduced into the system and is shifted below the laser focus as shown in Fig. 2.7(a), rays a and b are scattered upon the particle. Since the laser beam has a gradient intensity profile, rays a and b have equal light intensity. The emergence of the refracted rays a′and b′ caused a momentum transfer from the incident rays to the particle. The forces imparted by the rays are represented by $\mathbf{F_a}$ and $\mathbf{F_b}$, while the total force, $\mathbf{F_{total}}$ is the sum of vector forces. $\mathbf{F_{total}}$ in

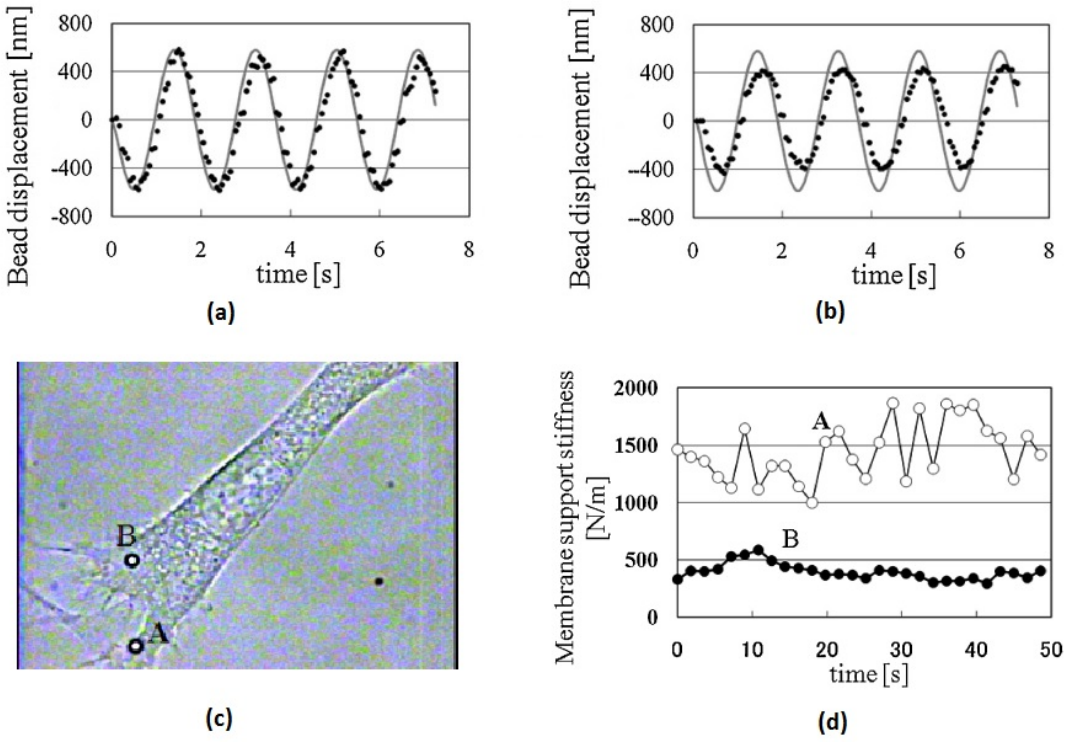

Figure 2.6: Results (a-b) Motion of particle manipulated by CPS. Solid lines indicate trajectories of the laser beam spot and dotted lines indicate motion of particle without adhesion and (b) with initial adhesion. (c) Bright field image of Balb3T3, and (d) Measurement of membrane support stiffness as a function of time, in which A and B graphs were obtained from the cell locales shown in (c). Images taken from [7].

this case, shows a backward trapping force component toward the beam focus. Similarly, when the particle moves above the laser focus as shown in Fig. 2.7(b), $\mathbf{F_{total}}$ still points toward the beam focus.

When a laser is focused on a particle, the particle will always experience a backward net force towards the beam focus. In order to manipulate a particle along the axial direction, the laser focus can be translated along the optical axis, which means changing the divergence of the laser focus [8, 90]. The same optics theory that changes the depth of the laser trap is applied using different techniques and devices. The next section will discuss three devices utilized in order to manipulate particles in the axial direction: motorized lens translation, deformable mirrors, and holography.

2.3.1 Techniques for axial displacement

In lens basics, by changing the spacing between two lenses, the resulting collimated beam can be made to be convergent or divergent, and visa-versa, as shown in Fig. 2.8. In a typical optical tweezers setup, this can be done in two ways: one is to focus the microscope up or down, in which the axial movement is accomplished because of the parfocality of the trap and specimen. Using this process, either the microscope can be motorized, or the sample (or the objective lens) can be situated in a vertical piezoelectric element. Another way is to change the parfocalizing optics. Given that the length separation between two lenses is approximately equal to the sum of the focal lengths of the two lenses, the control of one lens position can move the optical trap in depth (or axial direction) with respect to the specimen plane of the microscope [33]. Motorized lens translation offers the simplest way to axially manipulate the optical trap, and is quite stable (no drift) with lowest in terms of light loss [91–93]. However, for this type of setup, comparatively long lens translation is required because of several thousand axial reduction ratio of the optical path. Fällman proposed a design for a dual optical trap that is fully movable in the axial direction by creating two sets of afocal optical setup. The afocal setup can be constructed of either two positive lenses or one negative and one positive lens. Either one of the lenses can be moved to make the incoming laser beam divergent or convergent. Three dimensional piezoelectric stages also improve the precision and accuracy for mo-

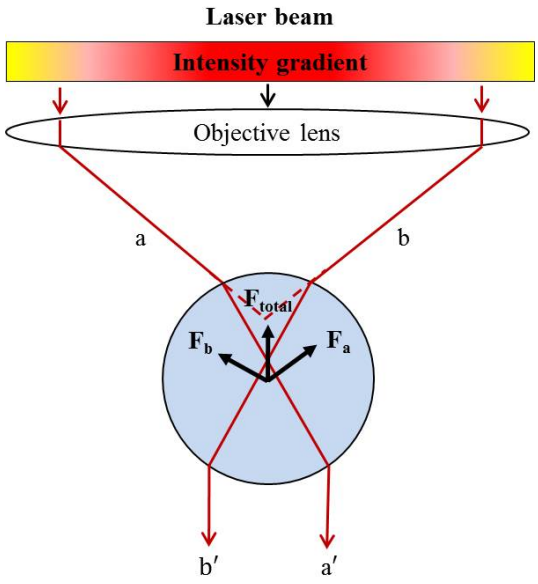

(a) Particle below laser focus

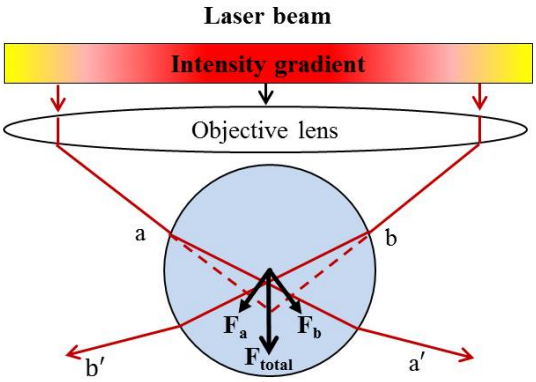

(b) Particle above laser focus

Figure 2.7: Ray optics diagram depicting how a focused laser maintains equilibrium even when the particle is displaced axially from the laser focus. Image based on [5]

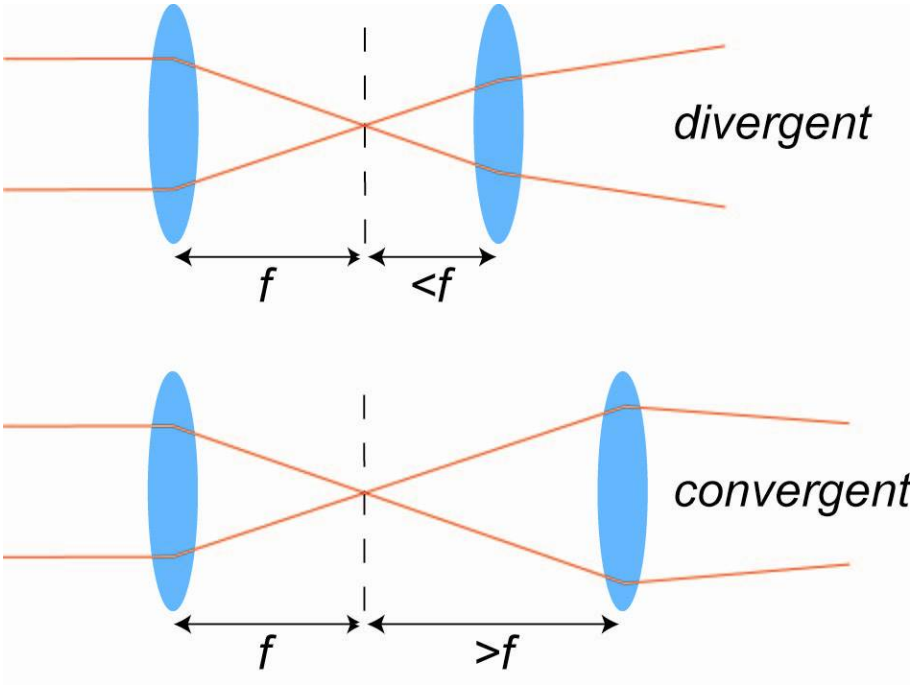

Figure 2.8: By placing the lens closer than the sum of the two focal lengths, a telescope can make the impinging light more divergent. If the lens are a larger distance apart, the beam becomes more convergent [8].

torized lens translation. Zhong implemented the motorized lens translation and measured the three dimensional trapping stiffness at different depths using image information entropy signals.

To improve the speed of control and overall precision of axial movement of the optical traps, deformable mirrors are utilized [94, 95]. Briefly, deformable mirrors modulate the wave front of an incoming laser beam by changing the shape of the mirror surface, as shown in Fig. 2.9. The wave fronts that control the shape of the deformable mirror are described in the Zernike polynomials, a complete and orthogonal polynomial set defined on the unit circle [96]. The fourth term called Zernike defocus term defines the deformable mirror shape for axial positioning [97]. In Ota paper, the maximum distance of the position change of a 1 μm polystyrene particle is 2370 nm, with minimum increment shift of 55.4 nm. Huang paper proposes an improvement of axial displacement

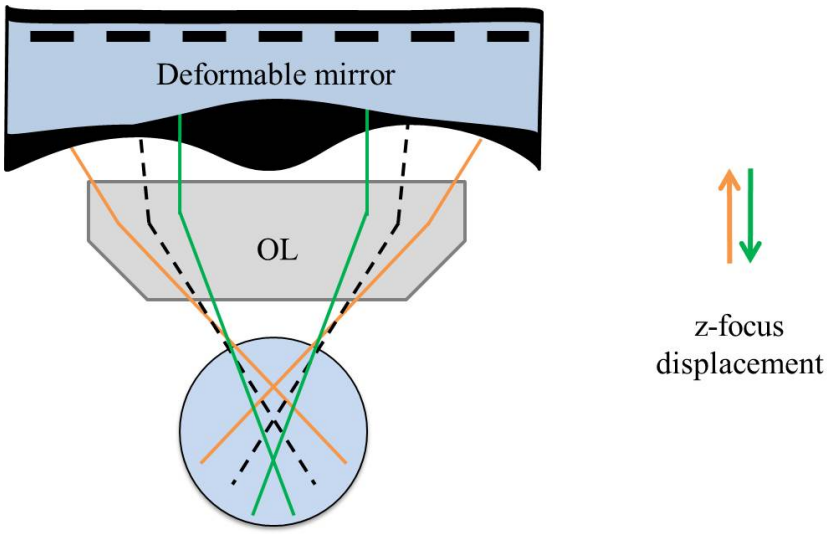

Figure 2.9: Wavefront modification for axial movement of optical trap using deformable mirrors. The orange rays denotes upward laser spot movement while blue rays show downward laser spot movement. OL: Objective lens. Image based on [9]

range through enhanced optical path design, modelling, and control. Using a 1.87 μm polystyrene particle, the result is a total axial steering range of 10.5 μm with error rate of less than 30 nm. The application of Zernike polynomials on deformable mirrors is not limited to position manipulation, it is also used for fast correction of aberrations in optical systems to improve trapping stiffness and forces [9, 98]. For example, Ota paper corrected the aberration by inducing the phase change described by the dominant spherical aberration mode, the 11th term in the Zernike polynomials. With the correction, the maximum trapping force exerted by a 1 μm-sized particle was increased. At 2 μm distance from the glass slide surface, the simulated trapping stiffness enhancement factor was computed as 1.20 and experimental enhancement factor was 1.35.

Another technique to create axial traps is to use diffractive optical components. This scheme is developed primarily to replace mirrors or acousto-optic modulators in creating multiple traps using a single laser source. When illuminated with plane wave, a simple grating produces multiple diffraction orders, providing a line of spots in the far field. The far field condition is obtained by inserting lens into the diffracted beams and imaging the intensity distribution at

its rear focal plane. Within optical tweezers, the microscope objective lens act as the transform lens. If the gratings are replaced by Fresnel lens, the diffraction order will be shifted out of the field, moving the trap axially. Because the diffractive optics is usually designed to convert a plane-wave, spatially coherent illumination into a specific intensity distribution in the far fields, these techniques are frequently called computer-designed holograms [90]. Liesener proposed the first full lateral and axial positioning using holographic optical tweezers. This is also the first reported work that three dimensional trap movement is made possible without moving parts. In this work, the computer-generated holograms are written on a liquid crystal display (LCD). After capturing the Fourier hologram images of 1 μm-sized particles using a CCD camera, the reconstruction is done by simply taking the Fourier transform of the holograms. The axial manipulation was made possible by adding a lens term to the blazed gratings or holograms [99]. Higuchi, on the other hand, focused on precise three-dimensional measurement of particle position using in-line digital holographic microscopy with green light emitting diode. An illustration of how in-line digital holographic microscopy records particle information is shown in Fig. 2.10. Low-coherence light was used to measure a 200 nm- and a 500 nm-sized particle because the scattered lights from the particles were very weak and were buried in speckles produced from unwanted scattered light. The axial positioning resolution computed is 3.4 nm [100].

2.4 Trapping stiffness and force measurement

In optical traps, the force is measured in conjunction with the stiffness of the trap. For small motions of a particle near the center of the optical trap, the forces acting on the particle approximate a linear spring at the trapping center [101]. However, as mentioned in the previous section, the scattering force actually pushes the particle in an area below the laser, thus measuring the trapping stiffness must be done with high accuracy. There are a number of methods that can determine the stiffness of optical traps such as power spectrum analysis, drag force method, and optical potential analysis [40]. Neuman review [102] provides a list of methods to measure trapping stiffness, wherein three, including the utilized method, are discussed in this section.

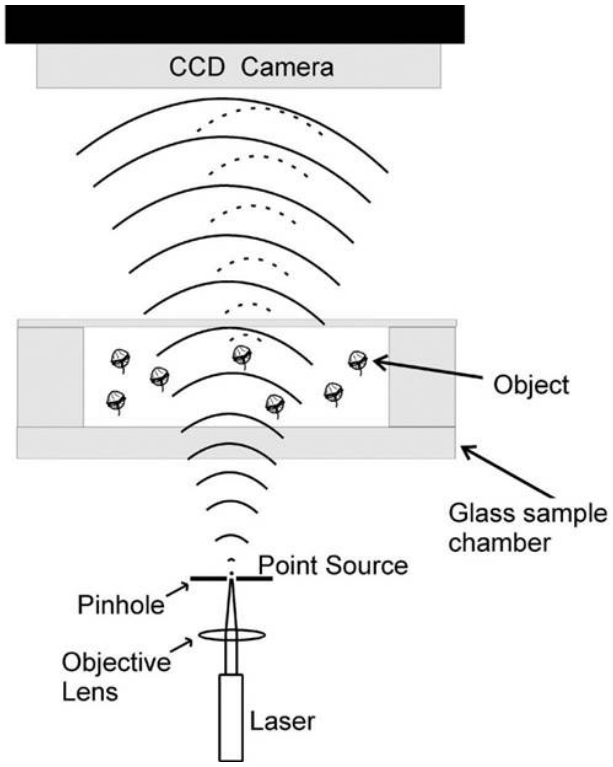

Figure 2.10: Schematic of digital inline holographic microscopy. Instead of taking the projected images of the object, the light wave front information from the object is digitally recorded as a hologram. First the laser is focused through the pinhole and the emerging spherical waves illuminates the objects. The interference pattern or hologram is recorded using detectors, in this case, a CCD camera [10] (http://fizz.phys.dal.ca)

Analysing the power spectrum of Brownian motion of a trapped particle provides the most reliable information about the trap [103]. The trapping stiffness is based solely on the rolloff frequency of the Lorentzian power spectrum (drag force of the particle being the only parameter to compute), making this method independent from position calibration. Moreover, the power spectrum of a trapped particle can serve as a diagnostic tool for optical trapping instruments; alignment errors of either the optical trap or the position detection system lead to non-Lorentzian power spectra, which are easily scored. And the extraneous sources of instrument noise lead to additional peaks in the power spectrum. This method can also monitor the sample heating due to partial absorption of the trapping laser light [104]. However, characterization and correction of the frequency response must be given sufficient attention to precisely measure the trapping stiffness. Other experimental effects such as anti-aliasing, insufficient bandwidth of photodetectors, surface effects, and viscosity also incorporate errors in the computation of trapping stiffness.

Another way to measure the trapping stiffness is to use a fluid chamber to compare the optical force with the force based on the viscous drag exerted by the fluid on the particle. The viscous drag force can be measured by Stoke's law [102, 105, 106]. This method is the most direct way to measure the trapping stiffness by generating fixed motions of the trap and measuring the displacement of the trapped particle from the equilibrium trap motion. Considerations arise in determination of drag coefficient and surface proximity corrections.

In this work, the equipartition theorem is utilized to compute the trapping stiffness. This method offers simplicity in its execution and computation. It is also not dependent explicitly on the viscous drag and height of the trapped particle, as well as the viscosity of the medium [102]. By observing the axial thermal fluctuations of a trapped particle, the trapping stiffness can be determined using the equation:

$$K = \frac{k_B T}{< z^2 >}, \tag{2.3}$$

where k_B is the Boltzmann's constant, T is the absolute temperature and z is the displacement of the trapped particle from the equilibrium position. Based on Eq. 2.3, the stiffness can be obtained by measuring the positional variance of a

trapped particle. The bandwidth requirements of the position detection system are the same as for the power spectrum method, but with the additional requirement of calibrated detector. Unlike the power spectrum method, the variance method does not provide additional information about the optical trap or the detection system. Variance method is also intrinsically a biased estimator (it is derived from the square of a quantity, and is therefore always positive). Any added noise and drift in position measurements serve only to increase the overall variance, thereby decreasing the apparent stiffness estimate. In contrast, low pass filtering of the position signal results in a lower variance and an apparent increase in stiffness [102].

After determining the trapping stiffness, the force exerted by the particle on the cell is measured using Hooke's law [90],

$$F = K\Delta z. \tag{2.4}$$

The force exerted on the cell could be measured in concurrence with the trapping stiffness, K, and the displacement from the trap equilibrium position Δz.

2.5 Methods for measuring elastic constant of cells

As discussed in the previous sections, the elastic constant of cells have been measured by a variety of nanomanipulation techniques. The discrepancies in the measured cell stiffness are expected from the myriad of techniques, and the different models used to describe the elastic constant of cells. Shear modulus measurement using optical traps can be computed based on different modelling approaches [107]. For example, the theory of Parker and Winlove [108] for elastic deformation of axisymmetric shells [22]. In particular, elastic modulus measurement using passive microrheology is based on Stoke's law [109,110], while a different model is tailored for micropipette experiments [111]. In this dissertation, the equation based on Hertz model, which is typically applied to AFM experiments, is applied to compute the localized cell stiffness.

2.5.1 Hertz model

For a homogeneous, semi-infinite elastic solid, the force-displacement is determined by two material properties, the Young's modulus E, and Poisson's ratio ν. The result for the force of the particle, or parabolic indenter, being exerted on a cell is related to the deformation depth δ via

$$F_{particle} = \frac{4}{3} \cdot \frac{E}{(1-\nu^2)} \cdot R^{1/2} \cdot \delta^{3/2}, \tag{2.5}$$

where R is either the radius of a spherical indenter, or the radius of curvature of a parabolic indenter.

Hertz model can also be applied when the indenter or probe has a conical shape:

$$F_{cone} = \frac{2}{\pi} \cdot \frac{E}{(1-\nu^2)} \cdot \delta^2 \cdot \tan(\alpha), \tag{2.6}$$

where α is the half-opening angle of the cone [79, 112].

To determine the elastic modulus E of cells, Eq. 2.5 will be utilized because the probes used in this dissertation are spherical particles with given radii. Given that the cell sample is virtually incompressible, ν can be set to 0.5 [113]. The rest of the quantities can then be measured experimentally.

Hertz model is a general model to measure contact mechanics with the following assumptions. Although some of the assumptions are not necessarily applicable to biological samples, the mechanical behaviour of cells often closely follow the hertz model prediction provided that experiments utilize low loading forces, and the cell locale is chosen with regards to the cell thickness [56, 114, 115]. Rahmat listed the assumptions:

1. The material of the contacting bodies is isotropic and homogeneous.

2. The loads applied are static. This assumption allows for the seismic dissipation of energy (vibrations or sound waves) during collisions between the two objects to be neglected.

3. The material is linearly elastic in nature. The constitutive law for the material behaviour is then considered to be Hooke's law.

4. The radii of curvature of the contacting bodies are much larger than the contact radius. Hertz theory is based on the problem of an elastic half-space (also called "semi-infinite sphere") subjected to surface tractions or pressures on a small localized area and zero tractions and displacements elsewhere on the surface.

5. The dimensions of the bodies are much larger than the dimensions of the contact surface. This assumption ensures that the stresses that arise due to the contact vanish at the opposite end of the body. The object should experience no tractions (or pressures) except at the contact surface.

6. The contacting surfaces are smooth. In other words no friction effects at the contact surfaces are considered.

7. The deformations are small. The theory is developed with an assumption of infinitesimal strains. Hence geometric non-linearities that arise due to large deformations are not considered.

Hertz model has been used for the cell poker and AFM techniques for the computation of the apparent stiffness of the cell [1]. In the cell poker experiments, certain issues prevent the results from having much significance. Some of these issues were the cell thickness being not much greater than the deformation depth, or the cell cytoskeleton was not an isotropic homogeneous material. Another problem is when the force is exerted on the sample, the force initiate biochemical and other active reactions [55]. In AFM, the Hertz model became widely used when a particle with well-defined geometry is attached on the tip of the device to address the homogeneity problem. Also, the force of the particle can be precisely exerted in particular cell surface locales and the corresponding displacements can be measured [43]. The nanometer displacement capability provides AFM the advantage over cell poker experiments in terms of controlling the indentation to be made on the sample. Finally, for the reactions of cells to exerted forces, AFM can be used in different modes to study, for example, the dynamic cell stiffening when probed with a rapidly oscillating tip [116, 117].

2.6 Chapter summary

Nanomanipulation plays a big role in biological applications, especially in cell mechanics and single-molecule force spectroscopy. Applying small forces on cells and other biological entities can provide information about the mechanical properties of cells. The cell elasticity, in particular, can offer insights about the cell structure, cellular reactions to outside mechanical stimuli, and functions of different cellular entities. The extracellular matrix and cytoskeleton are found to have contributed to the stiffness of targeted cell locales. The small displacements that can be performed and measured using different nanomanipulation techniques also give information about cellular walking and particle tracking within cells. DNA, RNA, and other proteins can also be manipulated in three dimensions.

Atomic force microscopy and optical tweezers are just two of the nanomanipulation techniques that are used for force spectroscopy and cell stiffness measurement. In AFM, a cantilever is used as probe to stimulate biological materials. A piezoelectric stage moves the sample towards the cantilever, while a laser is deflected off from the cantilever when the sample reaches the probe. A position detector measures the deflection of the cantilever. Force-curves derived from Hertz model provides the estimation of cell stiffness. Optical tweezers, on the other hand, is created using laser light that is focused using an objective lens with high numerical aperture to trap and manipulate particles in three dimensions. Ray optics diagrams are used to describe how the laser beam is able to stably trap small objects. A particular experiment is the Cell Palpation System (CPS). This method used an optical trapped particle to laterally probe a cell surface. The membrane support stiffness was measured from two different positions in the same cell sample, in which the positions gave different results. These findings elucidated that different cell locales have varying mechanical characteristics. To measure the cell stiffness in three dimensions, it is proposed that axial movement of optical trap will be integrated in the CPS.

In order to perform the axial movement of the optical trap, the spot focus must be shifted to change the divergence of the laser beam. This can be done using deformable mirrors, and spatial light modulators. The simplest way to incorporate axial movement is to use a motorized lens to change the spot position

along the optical axis. After finalizing the beam steering method, the equipartition theorem is chosen as the means to measure the trapping stiffness. This method studies the thermal fluctuations of a trapped object. Also called the variance method, the trapping stiffness is inversely proportional to the positional variance of the trapped particle. The force exerted on the cells is then computed using Hooke's law, wherein the force is proportional to the trapping stiffness and displacement from the equilibrium position. Finally, the literature about AFM provides the Hertz model that is used to measure axial cell stiffness while optical tweezers is the means of performing axial manipulation. The methodology of the proposed axial movement system is discussed in the next chapter.

Chapter 3

Axial manipulation system

The previous chapter provided a detailed discussion about the different studies that investigate the mechanical properties of cells. Examples of nano-manipulation techniques were also given. The devices used to axially manipulate the optical trap were also discussed. The Hertz model and the measurement of necessary parameters were tackled. In this chapter, the axial manipulation system (AMS) is discussed. Section 3.1 states the optical tweezers setup utilized for this work. The motorized lens control and data acquisition method are also described in this chapter. Section 3.2 to Section 3.4 show how the data, that is the particle images, are analysed to relate the z-focus position with the axial particle position. Section 3.5 states the experimental procedure, and Section 3.7 provides an examination on the overall performance of the proposed method. Finally, Section 3.8 summarizes this chapter.

3.1 Optical tweezers setup and axial manipulation method

The optical tweezers setup is shown in Fig. 3.1. The setup is based on an inverted microscope (Eclipse Ti-E, Perfect focus, Nikon Co., Japan). The laser beam is a Neodymium-doped yttrium aluminium garnet (Nd:YAG) laser (Spectra Physics Lasers, Japan), with wavelength of 1064 nm and maximum output power of 4 W. A high numerical aperture (NA = 1.2) 60x objective lens (Plan APO WI,

Nikon Co., Japan) focuses the laser beam to create a single optical trap. In Cell Palpation System, a set of galvano-mirrors reflects the laser beam to trap and move the particle in the lateral direction [7]. For the AMS, the lens L1 changes the laser spot position. Fig. 3.1(a) shows the axial movement of a particle. The lens L1 is translated to vary the laser spot position along the axial direction as shown in Fig. 3.1(b). The lens L1 is mounted on a stepping-motor that is connected to a computer via RS232. The stepping-motor is controlled using a LabVIEW program. Simply by changing the position of the lens L1 to axially move the trap, no major modification in the setup was made that could affect the lateral control of the optical tweezers.

A charged-coupled device (CCD) camera (WAT-920H, Watec Ltd., Japan) takes the images of the sample plane with shutter speed of 1 ms. The lens L1 program also commands the CCD camera to take an image after each lens L1 step. Other settings of the lens L1 program are enumerated in Appendix A.1. In this study, the lens L1 step is set to move in steps of 100 μm. The images taken at each step by the CCD camera provide granulated details regarding the movement of the particle. In effect, an image-based technique is utilized in this work, instead of quadrant photodiodes (QPDs). Although QPDs can obtain images at higher frequencies and can analyse particle movement with greater resolution, the field of view is limited compared with CCD cameras and other image-based techniques. Recent advances enable cameras and computers to obtain images at higher frame rates; from typical frame rates of 30-500 Hz, positional particle tracking is possible at greater than 6 kHz using CMOS camera [118]. Moreover, Image-based technique allows a wider area of study with reliable spatial homogeneity [90,119], a necessity when dealing with cell samples.

3.2 Image analysis

When the particle moves in the axial direction, the particle image becomes defocused. From this observation, the axial particle displacement can be related to the change in apparent particle size. To visualize and measure the apparent size of the particle, a separate program is created in LabVIEW Vision Builder. The image analysis program is divided into five processes, in which each step can be

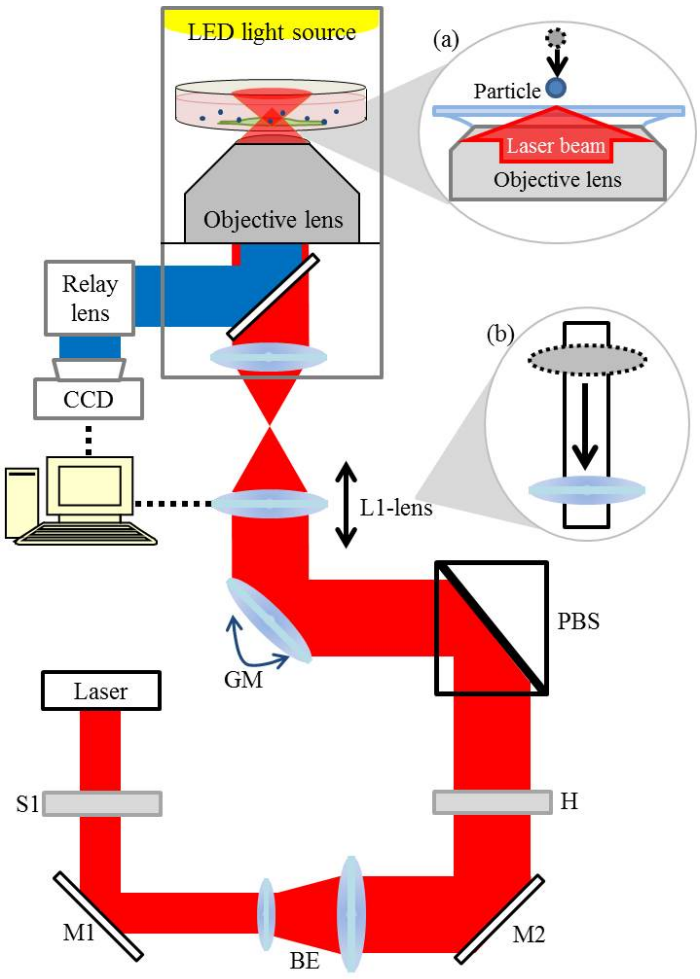

Figure 3.1: Schematic diagram of the optical tweezers setup. Inverted microscope; Beam source: Nd:YAG laser; S1: mechanical shutter; M1, M2: optical mirrors; BE: beam expander; GM: galvano mirrors; H: half wave plate, PBS: polarizing beam splitter. Inset: (a) Particle moves upward or downward (indicated as the change in z-axis) when (b) L1 lens is translated closer, or farther from the microscope, respectively.

modified as shown in Appendix A.2. The processes are as follows:

3.2.1 Acquisition step

The particle image in 8-bit TIFF file format is loaded into the image analysis program. The particle is then enclosed within a Region of Interest (ROI) as shown in Fig. 3.2(a).

3.2.2 Threshold step

Within the ROI, the threshold is adjusted to highlight the shape of the particle as shown in Fig. 3.2(b). The threshold is set to return dark objects since the pixel intensity value of the particle is less than the intensity value of the background pixels. The output binary image sets the pixels that are within the threshold range with a given RGB value (in this case, R=255) while the rest are set to zero value.

3.2.3 Filter step

Next, a local average filter in Fig. 3.2(c) rejects the outer ring and pixel noise. Until this step, the defocused particle image is emphasized. However, the change in apparent size is measured in terms of number of pixels.

3.2.4 Image calibration step

To measure the changing apparent size in real-world units, a particle image taken at the default lens L1 position is used as calibration image. The calibration image diameter is defined and is converted to the respective particle diameter utilized during the experiment. Then a reference axis is also defined. The apparent particle size can now be measured in terms of micrometers. This step is done only once and the result is integrated with the output of the next step, thus is not shown in Fig. 3.2.

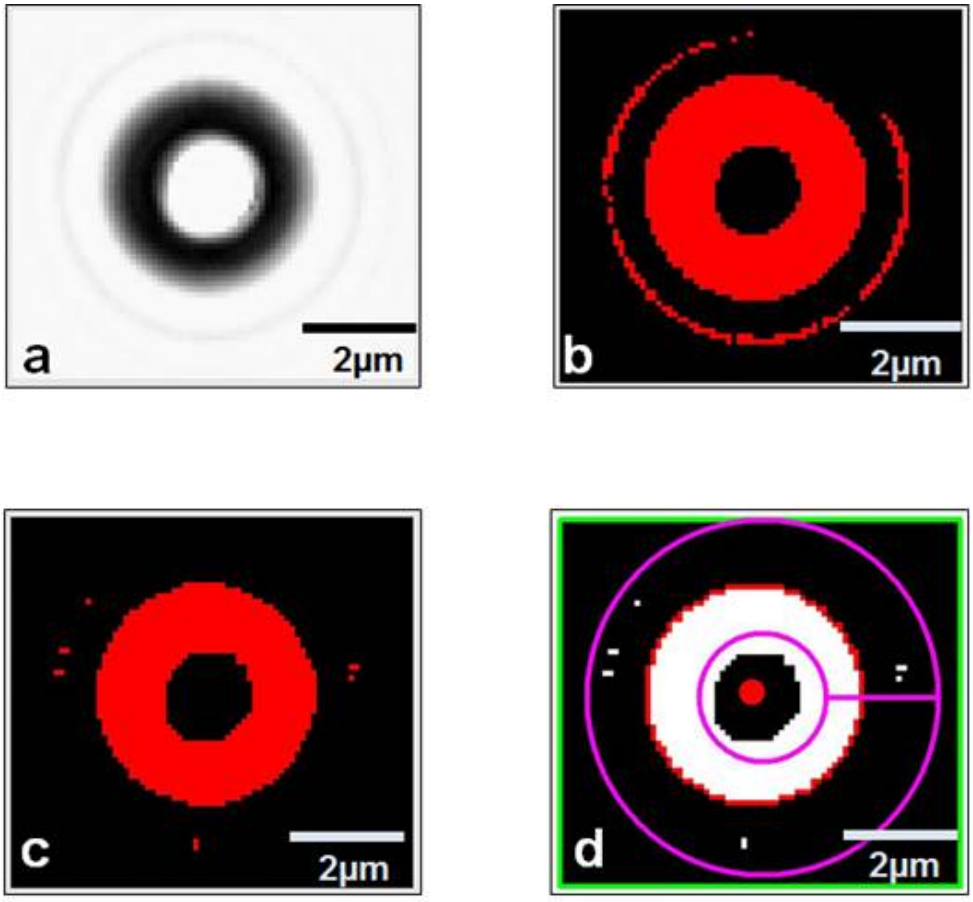

Figure 3.2: Sample image processing of particle. a) Raw particle image, b) threshold step: processed particle image, c) local average filter rejects the outer ring, and d) measurement of apparent particle size.

3.2.5 Circular edge detector step

A circular edge detector provides the best circular fit for the particle image by searching through the image for sharp transitions in pixel intensities. In this step, the pixel coordinates are transformed into the real-world coordinate through scaling in the x- (horizontal) and y- (vertical) directions. In Fig. 3.2(d), the connected concentric circles represent the range of viable area for measurement: an outline is extracted to approximate the particle circumference, and the dot represents the centroid of the particle. It is also possible to observe some random pixels that were not completely removed by the filter step. However, the viable area for measurement of the circular edge detector can be adjusted to only include the area of interest.

Effectively, the image analysis program can measure the particle position in three dimensions, but for this study, the horizontal and vertical changes of the particle position are disregarded. Only the change in apparent particle size is taken into consideration. The data log and processed images are saved in text file and JPEG-file format, respectively.

3.3 Calibration

From the image analysis, the relationship between lens L1 translation with the change in the apparent particle size is obtained. A calibration graph is created to form a basis for the axial particle displacement and apparent particle size. A particle fixed on a glass slide is observed. The objective lens is incremented by 200 nm using a piezoelectric stage (E-665.CR, PI GmbH and Co., Germany) and the apparent particle size is measured with each step. The minimum and maximum positions of the height of objective lens must encompass the subsequent changes in apparent particle size. To identify the necessary range of the calibration graph for the given lens L1 translation, the images and measurements of the calibration particle and lens L1 particle are compared. The calibration method is shown in Fig. 3.3(a) and the calibration graphs for a 4 μm-sized particle and a 2 μm-sized particle are shown in Fig. 3.3(b) and Fig. 3.3(c), respectively. The calibration graphs show a linear relationship between the height of the objective

lens and change in apparent particle sizes. The changing height of the objective lens serves as the changing axial displacement of the particles. Different stuck particles observed and shift in objective lens height account for the discrepancy from linearity and sharp increase in the particle size, notably in the 2 μm-sized particle. As such, some points in the 2 μm-sized particle are omitted to extract a linear equation suitable for calibration purposes. The sensitivity of the image analysis program is computed; that is, the program can detect 15 nm change in apparent particle size.

3.4 Position analysis

Subsequently, the linear equations of the calibration graphs for the corresponding particles are computed. These equations relate the lens L1 translation with the axial particle movement [40]. From these converted graphs, the change in laser spot, or laser z-focus position, are computed. Because the lens L1 is translated in increments of 200 nm, the z-focus position is expected to increase in uniform steps. The gradient of the axial displacement as a function of lens L1 translation provides the respective step size. To validate the results, the length of the z-focus displacement should correspond to the length of axial particle displacement.

3.5 Experiments

The axial particle displacement experiments are conducted using 4 μm-sized particles and 2 μm-sized particles. These particle sizes are chosen based on biological limitations and technical limitations of the proposed system [7, 22, 25, 27, 28, 107, 120–123]. The particles are placed in separate glass slides. From the default position in the optical setup, the lens L1 is translated closer, and then farther, from the objective lens for 150 steps (with 100 μm movement per step). The corresponding movements of the z-focus spot are upward and downward, respectively. Next, the initial position is shifted, then the lens L1 is translated for the same number of steps. The experiments will elucidate on four purposes of this system: (1) determine the sensitivity of the system in terms of detecting the axial particle displacement. Also, (2) the initial lens L1 position is investigated to determine

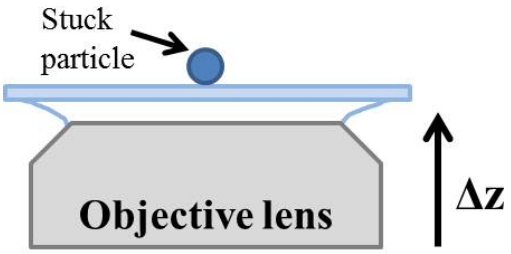

(a) Illustration of calibration method

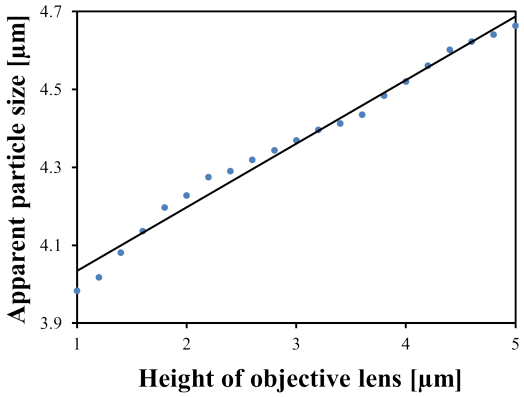

(b) 4 μm-sized particle calibration graph

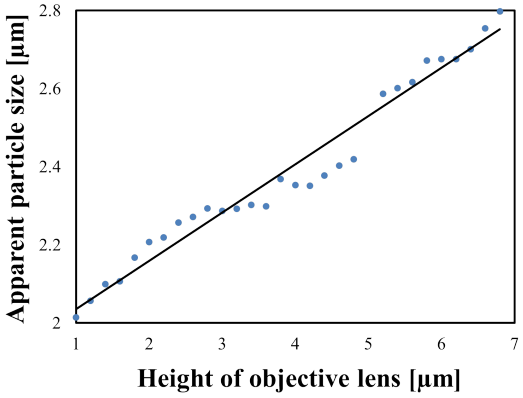

(c) 2 μm-sized particle calibration graph

Figure 3.3: Calibration method of the axial particle movement. (a) A particle stuck on the cover glass is observed. The axial movement is based on the changing height of the objective lens. (b-c) The calibration graphs show the relationship of the height of the objective lens with the changing apparent size of the defocused particle image.

the range of possible axial particle displacement, and (3) to determine the linear region of the particle displacement. Finally, after obtaining the results from the first three purposes, (4) a comparison between the axial displacement of the two different-sized particles is conducted.

3.6 Results

Sample particle images at a given lens L1 position are shown in Fig. 3.5. In terms of visualizing the image, the results showed that as the particle was moved in the axial direction, the particle became defocused. The 4 μm- and 2 μm-sized particles exhibited similar defocused characteristic: from the particle having a thicker shape, the particle image grew thinner as the particle was moved downward. However, the smaller particle images in Fig. 3.5(d-f) were overall more defocused than the bigger particle images.

Graph results of axial particle movements at different initial lens L1 positions are shown in Fig. 3.4. Manipulating the particle at different initial positions of the lens L1 provided an illustration of the range of possible particle displacement, as well as showed at which initial lens L1 position the z-focus position and axial particle position would result in a linear relationship. It was also noted that the upward motion exhibited less particle movement compared with the downward motion, which was apparent in the 4 μm-sized particle in Fig. 3.4(a). This occurrence denoted that the movement of the axial particle position did not correspond to the movement of the z-focus position because the z-focus position was theoretically moved with the same length, although in opposite directions. Further details on the results are discussed as follows:

3.6.1 4 μm-sized particle

The first initial position of the lens L1 shown in Fig. 3.4(a) was at the default position of the optical tweezers setup. For clarity, the lens L1 default position will be assigned as 0 μm z-focus position. The upward motion, indicated as green line in the legend, gave a linear graph from 0 μm to approximately 2.5 μm z-focus position. However, the downward motion provided an unclear relationship of axial particle position and z-focus position. The graph is not included in this

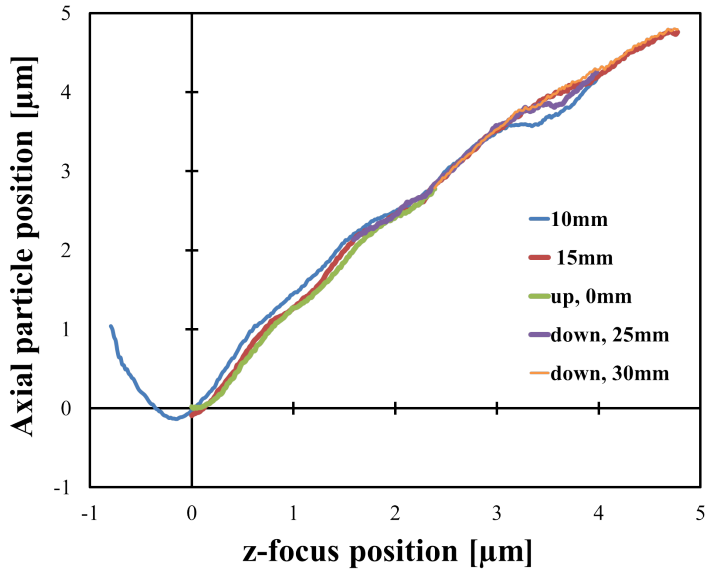

(a) 4 micron

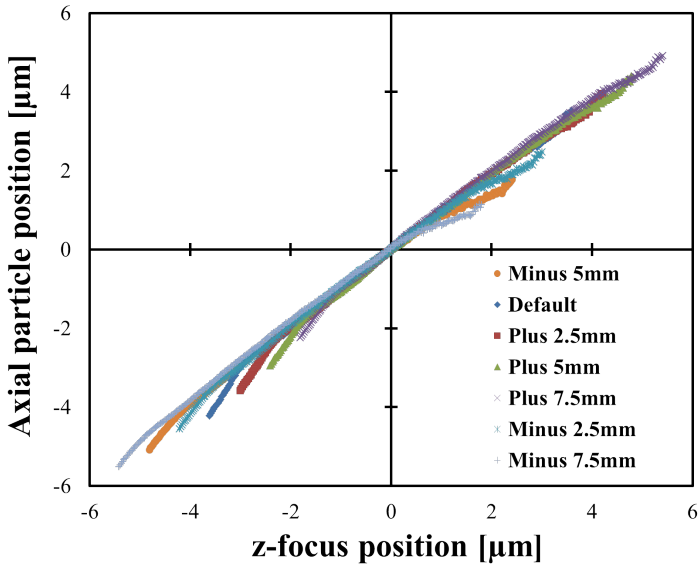

(b) 2 micron

Figure 3.4: Results for particles at different initial lens L1 position. Changing the initial lens L1 position results in different graph characteristics, as well as greater downward particle movement than the upward particle movement, as seen in the 4 μm sized particle in (a). For the 2 μm-sized particle in (b), the results show similar graph characteristics in terms of linearity. However, the downward motion of the z-focus position also exhibited more particle movement than the upward motion.

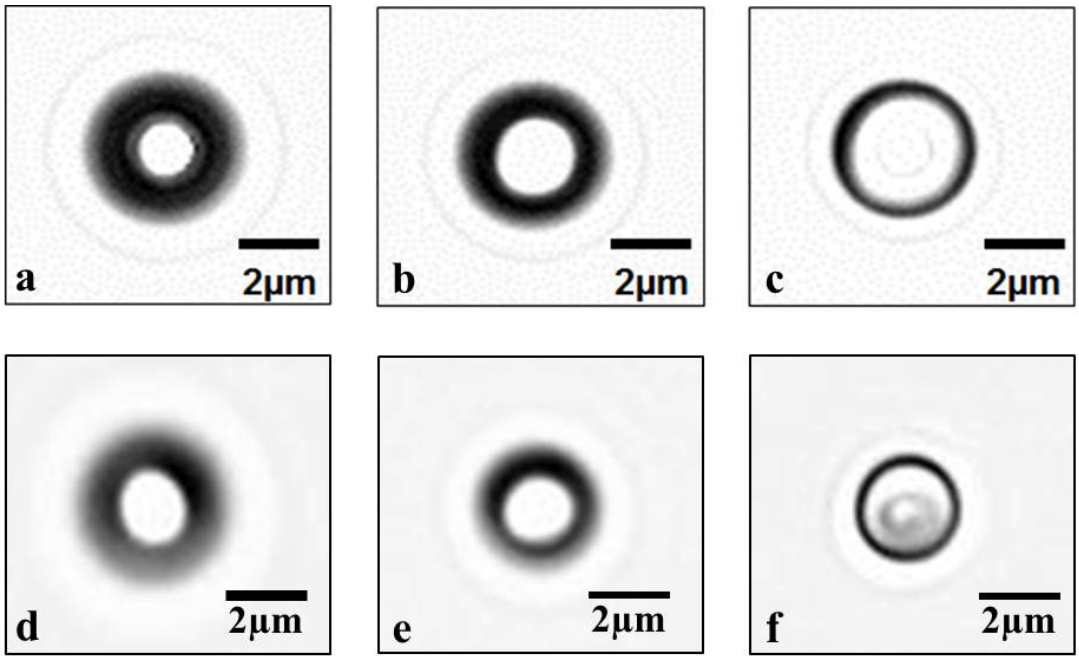

Figure 3.5: Sample images of particles moved downward. The negative sign describes the downward movement of z-focus position from the initial (or zero) z-focus position. 4 μm-sized particle at (a) initial or 0 μm laser z-focus position, (b) midway or approximately -1.3μm laser z-focus position and (c) approximately -2.5μm laser z-focus position. 2 μm-sized particle at (d) initial or 0 μm laser z-focus position, (e) midway or approximately -1.5μm laser z-focus position and (f) approximately -3μm laser z-focus position.

dissertation, however, this ambiguous occurrence also appeared in the downward motion of another graph.

When the initial lens L1 position was changed to 10 mm closer to the objective lens indicated as blue line, this resulted to the shift of initial z-focus position from 0 μm to 1.6 μm and with final z-focus position at around 4 μm. The upward motion initially exhibited the same behaviour as the upward motion from the default lens L1 position. However, an inconsistency from a linear relationship occurred at laser z-focus position from 3 μm to 4 μm. The downward movement also exhibited unclear data. This could be explained by studying the raw data and recalling the complete calibration graph of a particle from [124].

The procedure for creating the calibration graph from [124] was as follows: first, the objective lens was focused "lower" than the particle, giving a very defocused image of the particle. The height of the objective lens was then incremented until the particle becomes focused. Afterwards, the objective lens height was incremented further until the particle became out of focus again. The result was a graph that started from a larger apparent particle size, that became smaller as the objective lens was incremented. Then the size became bigger again after reaching the focused image with increasing objective lens height. To remove the ambiguity, only one side of the calibration graph was taken into account, as also shown in this dissertation in Fig. 3.3(b-c).

Based on this characteristic of defocused-focused-defocused particle image as the particle moves axially, the downward motion from initial lens L1 position at 10 mm (and from default lens L1 position) started from defocused particle images but went beyond the focused image. Thus the axial particle position did not move up as the z-focus position was moved further down, rather, the particle also moved downward. But because the calibration graph dictates a linear relationship between the change in apparent particle size and axial particle movement, the graph of initial lens L1 position at 10 mm in Fig. 3.4(a) showed an incorrect position estimation.

Red line indicated the shift of initial lens L1 position to 15 mm closer to the objective lens, resulting in an upward shift of the initial z-focus position to 2.4 μm. The final axial particle position for the downward motion was at 0 μm. The final particle position was expected because this was simply a reflection of the upward

particle motion from the default lens L1 position. As such, the characteristics were similar. On the other hand, the final axial particle position for the upward motion was at 4.8 μm. Although the graph overlapped with the 10 mm-shift of initial lens L1 position, the inconsistency was not observed.

To understand the discrepancy from a linear regression that occurred at laser z-focus positions from 3 μm to 4 μm, the z-focus position was placed at 4 μm, and was shifted downward as indicated by purple line. This experiment verified if the discrepancy is inherent in the setup and results, or if it was caused by errors. The result shows a decrease in the range of discrepancy from 1 μm to 0.5 μm. The discrepancy also shifted at z-laser position from 3 μm to 3.5 μm.

Finally, a shift in the initial lens L1 position from default position to 30 mm closer to the objective lens resulted in the upward shift of z-focus position from 0 μm to 4.7 μm. The particle was then moved downward to investigate the consequent particle movement from the downward movement of laser z-focus positions from 4.7 μm to 2.4 μm. The result, depicted as orange line, shows a similar graph characteristic with the upward motion of the graph with 15 mm-shift in the lens L1 position. The inconsistency in question was not evident.

It is possible that the inconsistency stemmed from the inability of the setup to stably trap the particle from a particular initial lens L1 position, especially for the graph with initial lens L1 position at 10 mm closer to the microscope (blue graph). It can be observed that the inconsistency appeared at the latter end of the observed graph. As for the graph with initial lens L1 position at 25 mm closer to the microscope, the decreased inconsistency could be caused by mechanical drifts in the system.

3.6.2 2 μm-sized particle

Based on the results from the bigger particle experiments, the experimental procedure for the 2 μm-sized particle shown in Fig. 3.4(b) had been modified in terms of choosing the initial lens L1 position. Because the particle image is more defocused thus it is more prone to image distortion. The first experiment was to obtain the axial particle positions when the particle is moved upward and downward from the default lens L1 position. At initial lens L1 position, the z-focus position was at 0 μm with axial particle position normalized at 0 μm. The

normalization was necessary to differentiate the upward particle motion, which is depicted in the positive z-focus translation and axial particle movement. On the other hand, the negative values depict the downward z-focus translation and corresponding downward particle movement. The final z-focus position was at 3.4 μm for the upward motion, wherein the corresponding upward axial particle position was 3.6 μm. The final z-focus position for the downward movement was -3.4 μm, with downward particle movement from 0 μm to -4.2 μm. Similar with the bigger particle, the upward particle movement was still shorter compared with the downward particle movement, although the z-focus movement was the the same, just in opposite directions.

The axial particle movement with initial position at the default z-focus position resulted to a linear relationship as depicted by the purple graph. Interestingly, all the graphs from different initial lens L1 positions resulted to almost similar characteristics and approximately the same range of axial particle movement (7 μm to 8 μm in axial particle movement). The uppermost axial particle positions were distorted, while the lowermost axial particle positions smoothly moved downward, yet deviated from the linearity of each graph. The remaining results will be briefly described below:

At initial lens L1 position shifted 7.5 mm closer to the objective lens (dark blue graph) from the default lens L1 position, the corresponding initial z-focus position shifted to 1.8 μm. The final upward z-focus position was at 5.4 μm. The upward particle movement was from 1.8 μm to 5 μm. On the other hand, the final downward z-focus position was at -1.8 μm with downward particle movement from to 1.8 μm to -2.2 μm.

Shifting the lens L1 position 5 mm closer to the objective lens (red graph) resulted to shifting the z-focus position from 0 μm to 1.2 μm upward. The maximum upward z-focus position was at 4.8 μm. The particle movement obtained from moving the particle upward was from 1.2 μm to 4.4 μm. For the downward movement, the maximum z-focus position was -2.4 μm, with particle movement from 1.1 μm to -3 μm.

With the lens L1 translated 2.5 mm closer to the objective lens (green graph), the initial z-focus position was shifted 0.6 μm above the default z-focus position. The overall z-focus movement was from -3 μm to 4.2 μm, with corresponding

axial particle movement from -3.6 μm to 4 μm.

When the lens L1 was shifted 2.5 mm farther from the objective lens (light blue graph), the initial z-focus position was translated to -0.5 μm.The lowest z-focus position reached was -4.2 μm with corresponding -4.5 μm particle movement. On the other hand, the maximum upward z-focus translation was 3 μm, with maximum upward particle movement reaching 2.7 μm.

For the shift of -5 mm from the default lens L1 position (orange graph), the initial z-focus position was -1.2 μm wherein the initial particle position was situated at -1.1 μm. The lowest to highest shift of z-focus position was from -4.8 μm to 2.4 μm, with corresponding particle movement from -5.1 μm to 1.8 μm.

Finally, shifting the lens L1 position by -7.5 mm (light purple graph) resulted in a shift of z-focus position to -1.6 μm. The maximum downward z-focus position was -5.4 μm with corresponding final downward particle position at 5.5 μm. The maximum upward z-focus position was 1.8 μm, with corresponding maximum upward particle position at 1.1 μm.

3.6.3 Comparison of 4 μm and 2 μm-sized particles

The difference in the defocused images of the 4 μm- and 2 μm-sized particle as shown in Fig. 3.5 was attributed to the decrease in pixel counts and contrast of the particle with the background. The experiment with the 4 μm-sized particle was conducted first, and then the sample with 2 μm-sized particle was used. The illumination and magnification setting from the former particle were adjusted to compensate for the smaller size of the latter particle. In the case of 2 μm-sized particle, the relay lens was used to detect the small changes in axial particle position. The introduction of the relay lens magnified the lower contrast between the smaller particle and background. However, using the relay lens to magnify the 4 μm-sized particle caused two things: Firstly, the ROI could not encompass the change in apparent particle size when the particle is moved in the axial direction, and secondly, multiple fringes of the particle image were emphasized thus the image analysis program suffered from increased noise. In this case, the 4 μm-sized particle images were taken without the relay lens.

The lens L1 translation step of 100 μm was constant for both particle experiments. But the z-focus translation step was different by 50 %. For the 4 μm-sized

particle, each lens L1 step corresponded to 16 nm step of z-focus position, while each lens L1 step was equal to 24 nm z-focus step for the 2 μm-sized particle. The difference in the computed z-focus step also explained the increase of particle movement for the smaller particle: the average axial particle movement for the 4 μm-sized particle was 5 μm while 2 μm-sized particle had an average of 7.5 μm.

Given 150 steps of lens L1 translation, the 2 μm-sized particle provided slightly higher linear characteristics. The calculated linear coefficient of determination, R^2, for the graph with initial lens L1 position at the default position was 0.99. For the 4 μm-sized particle, the graph with initial position shifted 15 mm closer to the objective lens provided the highest computed R^2 of 0.98. These aforementioned graphs will be considered as the linear regions for further experiments. Although, for the 2 μm-sized particle, the z-focus translation will be shorten to move from -3 μm to 3 μm to improve the linearity. The axial displacement of the 4 μm-sized particle will be retained.

3.7 Discussion

The particle sizes used in the experiments showed us the capabilities and limitations of the proposed system. Typical experiments with cells use 1 to 10 μm-sized particles. However, the optical tweezers setup used in this work had a maximum resolution of 10 μm. Given that the particles will be attached on cell surfaces, smaller particles are considered. Bigger particles exhibit multi-fringes compared with smaller ones, making it difficult to measure the apparent particle size. And as seen in the results in Section 3.6, the bigger particle exhibited ambiguity when the initial lens L1 was moved, and could only be manipulated for 5 μm. On the other hand, the 2 μm-sized particle showed linear regions at longer ranges without exhibiting the said ambiguity. It was also difficult to detect the very small movements of 1 μm. From these points, a 3 μm-sized particle may also offer interesting results in future work.

Using the system, the linear regions in both the upward and downward translation of trapped particle were determined. However, the difference in the particle displacement from the upward and downward graphs may be due to spherical aberrations, viscous drag force, and mechanical errors. The results obtained

from the calibration and axial particle displacement experiments answered the four questions raised in this chapter. However, various issues were also observed.

Firstly, it is important to set the initial particle size in order to formulate the equation and method for the axial particle position estimation. In this dissertation, the calibration graph was set to consider the defocusing images of the particle from the focused image (smallest apparent particle size) until the defocused images taken at the highest possible objective lens height. Effectively, this provided the assumption that particle images with bigger apparent size is positioned higher than a particle with smaller apparent size as shown in Fig. 3.3. Further experiment and data regarding the apparent particle size at lower objective lens height than the focused image were not included in the results.

In connection to the previous paragraph, the initial particle image at the initial z-focus positions revealed different particle image for the 4 μm- and 2 μm-sized particle. The shift in initial particle images caused a different interpretation of particle displacement observed at the same lens L1 position. This is seen at Fig. 3.4(a) where the 4 μm-sized particle went beyond the focused particle image causing the incorrect evaluation of axial particle position from -1 μm to 0 μm laser z-focus position. Fig. 3.4(b) revealed that at different lens L1 position, the 2 μm-sized particle was well within the range of specified calibration graph. The non-linearity encountered with the bigger particle was not evident in the small particle.

Thirdly, regarding axial particle displacement range, the lens L1 translation was set to move 150 steps because the change in apparent particle size could be visually observed from the CCD camera, without sacrificing the time it takes for the system to capture the images. Shorter lens L1 translation experiments were also conducted, yet a longer range of observable axial particle displacement is more desirable, especially for biological applications.

Finally, the movement of the z-focus position was not consistent with the movement of the particle position, possibly due to spherical aberration. It was surmised that when the particle is manipulated, the movement of the particle deviates from the movement of the (laser) z-focus because the laser beam is not perfectly focused at one point.

Overall, in measuring the axial particle movement, the defocusing of the par-

ticles was observed. This means that the illumination of the particles and the stability of the system are important points to address. As a precaution, the experiments were carried out in series as to decrease the probability of changing the illumination level. Then, for every new dataset obtained, the image analysis program was recalibrated and rechecked with previous datasets. The relative ease of use of the system and minimum handling of the setup provided the opportunity to create a stable system, wherein the only considerations were the mechanical drift of the objective lens and the stage, and the adjustment of laser power. These errors were compensated through extracting large datasets to verify the results obtained, thereby reflecting the capability of the designed system.

3.8 Chapter Summary

This chapter covered the axial manipulation system. The proposed system can manipulate particles along the optical axis by translating one of the optical component called lens L1. The system then measures the particle position using a calibration graph as basis for axial particle position. The experiments include axially moving the particle for 15mm lens L1 translation, and changing the initial lens L1 position.

The fours purposes attained in this chapter are:

1. **To determine the sensitivity of the system in terms of detecting the axial particle displacement**

   The sensitivity of the system is computed from measuring the fluctuations of a fixed particle to the cover glass in Section 3.3. The fluctuations are caused by Brownian motion and mechanical drifts of the system.

2. **To investigate the initial lens L1 position to determine the range of possible axial particle displacement**

   The possible range of axial particle movement must comply with the two assumptions: First, the axial particle position as a function of laser z-focus position must have a clear relationship, as explained in Section 3.7. And second, a linear relationship between the two parameters is desired. For

the 4 μm-sized particle, the range is 5 μm. On the other hand, the 2 μm particle can be axially moved for 12 μm.

3. **To determine the linear region of the particle displacement**

   For the 4 μm-sized particle, the linear region is determined as the graph with initial lens L1 position set 15 mm closer to the objective lens, and the corresponding z-focus position is set as 0 μm. For the 2 μm-sized particle, the linear region is determined by the computed R^2 value, in which the z-focus position is set as 0 μm when the initial lens L1 position is at the default lens L1 position. However, the upward motion of the particle exhibits longer particle movement than the downward particle movement even though the z-focus is moved in the same length downward and upward.

4. **To compare the axial displacement of the two different-sized particles**

   Three points of comparison are raised for the two different-sized particles. First, each particle shows different image characteristics when trapped at the default lens L1 position. This observation is further validated when each particle is axially moved downwards. The 4 μm-sized particle goes beyond the focused particle image, while the 2 μm-sized particle remained within the assumed linear region. Second, the corresponding laser z-focus position per lens L1 step varies for the two particles utilized in the experiment. Each lens L1 step is equal to 16 nm laser z-focus step for the 4 μm-sized particle, while each lens L1 step corresponds to 24 nm laser z-focus step for the 2 μm-sized particle. Finally, regarding the linearity of axial movement the two different-sized particles, both have high R^2 values, which validates a linear relationship between z-focus movement and axial particle movement, although the positions have irregularities.

From these results, the proposed system can be used to axially manipulate particles. The linear regions were obtained for subsequent experiments. The 4 μm-sized particle will be set to move from initial lens L1 position at 15 mm closer to the microscope, and the z-focus will be axially moved for 5 μm. For the 2 μm -sized particle, the initial lens L1 position will be set at the default

position, and the z-focus will be moved for 6 μm. In force spectroscopy, particles are typically used as probes to mechanically exert forces on biological materials. Computing these forces can provide insights on the mechanical properties of cells.

The following chapter will discuss the application of the axial manipulation system to biological materials. Specifically, the system will be used to measure the localized cell stiffness of Balb3T3.

Chapter 4

Measurement of cell stiffness

The previous chapter gave a thorough discussion on how the proposed axial manipulation system traps and moves a particle in the axial direction. The optical tweezers setup and axial particle position estimation were also explained. The results provided the initial lens L1 position that can give the most linear relationship between the z-focus position and particle position. The purpose of this chapter is to describe the application of the proposed system in measuring the mechanical properties of cells. First, the force exerted on the cell by a trapped particle is measured. The cell force measurement will include the computation of trapping stiffness using equipartition theorem. The localized cell stiffness of a Balb3T3 sample will then be evaluated using Hertz model equation.

In effect, there will be three major sections. For clarification, each experiment, that is, the (1) trapping stiffness, (2) cell-force measurement and (3) localized cell stiffness measurement, will be discussed in succeeding sections. Each methodology and results are incorporated in the respective sections. Another section will give the discussion of the overall biological application of the proposed system and finally, a chapter summary will be provided.

4.1 Sample preparation

For the trapping stiffness experiments, carboxyl polystyrene particles (Spherotech, Inc., USA) with 4 μm and 2 μm diameters are each diluted in distilled water and are placed on glass slides. For the cell experiments, cell samples will be prepared

as follows: mouse fibroblast (Balb-3T3) cells are cultured in Dulbecco's modified eagle medium (DMEM) supplemented with 10 % fetal bovine serum (FBS), 1 % penicillin and streptomycin solution at 37 °C and 5 % CO_2. On the third day, the samples are washed with phosphate buffered saline or PBS twice and the medium is changed. After two days, 80 % confluent cells from the sample are treated with trypsin-EDTA for 2 minutes and are collected via centrifugation at 1500 rpm for 5 minutes. 35 mm glass bottom dishes are treated with collagen and air dried for at least 30 minutes prior the sample passage. These dishes are washed twice by 2 mL PBS to remove the acid. Then, the cells are re-suspended in cultured medium and are placed in the collagen coated dishes. On the day of the experiment, the medium is removed and the samples are washed with 2 mL PBS. Afterwards, fresh medium is added on the samples. 100 μL of collagen coated particles (Micromod, GmBH and Co., Germany) with diameters 4 μm and 2 μm are diluted 10000 times and are added into different cultured samples. The samples are left at room temperature for 5 minutes in order for the particles to settle close to the cells.

4.2 Trapping stiffness measurement

To determine the axial trapping stiffness using Eq. 2.3, the movement of the fluctuating trapped particles are measured. The positional variance (square of standard deviation) of trapped particle as a function of laser power is obtained. First, laser is set to minimum power and the CCD camera captures a total of 2000 images of the trapped particle. Afterwards, the variance is computed. This process is repeated for an interval of laser power until the images are taken from the maximum laser power. Since the axial movements of the trapped particle are very small and fast, the magnification of the image is increased using relay lens. The laser power is measured at the exit of the objective lens to obtain a precise value of the laser power experienced by the particles. The results for the standard deviation of the fluctuating particles and trapping stiffness are shown in Fig. 4.1.

Fig. 4.1(a) shows the standard deviation of the fluctuating movements of the trapped particle. At laser power less than 5 mW, particle movements for

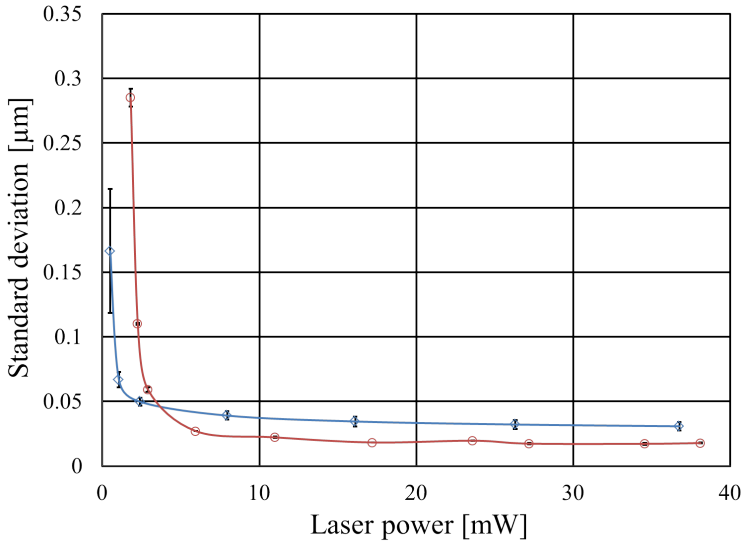

(a) Standard deviation

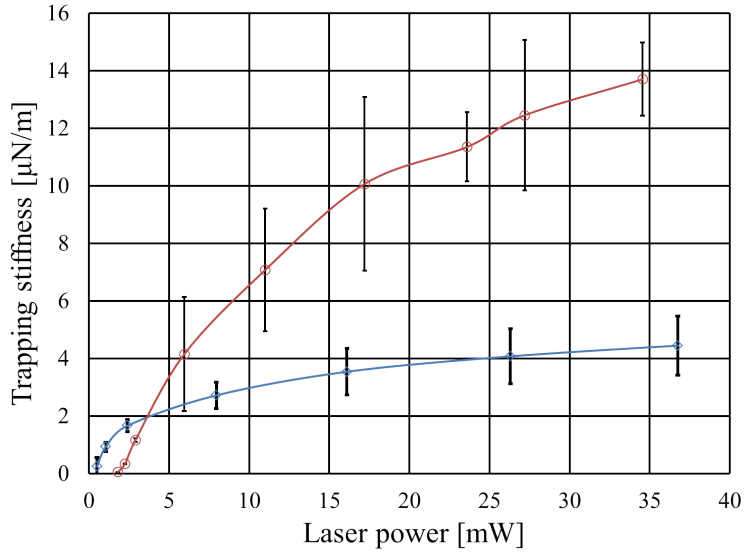

(b) Trapping stiffness

Figure 4.1: Comparison of the measured fluctuating trapped particles. Blue line represents results for 4 μm-sized particle and red graph represents the results for 2 μm-sized particle. (a) Standard deviation. At lower laser power, trapped particles exhibit greater fluctuations. (b) Trapping stiffness. The trapping stiffness value is lower for the 4 μm-sized particle than the 2 μm-sized particle.

both particles (Blue and red graphs represent 4 μm- and 2 μm-sized particle, respectively) had considerable values. These results were also validated during experiments when the particle images showed visible random movements. But at laser power greater than 5 mW, both graphs began to stabilize. Particle movements also became obscured visually.

Based on Eq. 4.2, the variance is inversely proportional to trapping stiffness. It was expected that the values of the standard deviation of trapped particle fluctuations were greater at lower laser power and the trapping stiffness values were smaller at lower laser power. The trapped particle fluctuations stabilized at different laser powers; For the 4 μm-sized particle, the particle movement stabilized the laser power at 36.8 mW, in which the trapping stiffness was computed to be 4.5 $^{\mu\mathrm{N}}/_{\mathrm{m}}$. The 2 μm-sized particle stabilized at 23.6 mW, and the trapping stiffness was computed to be 11.4 $^{\mu\mathrm{N}}/_{\mathrm{m}}$. These laser power values were utilized for the axial displacements of unattached particles experiments and for the cell-attached particles experiments.

Trapping stiffness measurement discussion

As mentioned in Section 2.4, equipartition theorem is a biased estimator, hence noise and drifts in the position measurement greatly affect the positional variance. This will then result to inaccurate trapping stiffness measurements. Preliminary experiments for measuring the positional variance revealed three main difficulties. In this section, these problems are tackled. First problem was the undetected small axial particle movements. This was especially experienced when dealing with the smaller particle. As mentioned, the relay lens had been used to magnify the particle images, however, the standard deviation of the measured fluctuating particle position were still too low. This was solved by adjusting the shutter speed of the CCD camera and setting the lighting condition, i.e., the background, to become lighter so that the particle image was emphasized. The image analysis program, specifically the threshold setting, was also adjusted accordingly.

The second problem was the appearance of spikes shown in Fig. 4.2(a), which happens when the lighting condition suddenly changes. Possible explanation of lighting changes is when a free particle comes in between the trapped particle and LED light source. The slight darkening of the image affects the trapped particle

shape at that instance thus the measured axial particle position is slightly bigger. However, outliers are apparent in all experimental data, thus proper filtering was necessary to remove outliers.

Finally, the third problem was observed during the initial gathering of data set. During preliminary experiments, the CCD camera was set to take 250 images per laser power, with total image acquisition time of 120 seconds. It was observed that for a particular set of data, the data became skewed as seen in Fig. 4.2(b-c). The drift in objective lens might have caused this particular error for Fig. 4.2(b). Recall from Section 3.3 that the apparent particle size was assumed to have a linear relationship with axial particle position. In the trapping stiffness experiments, some trapped particles are pushed out by another particle with slightly different size. The slight change in apparent particle sizes would then have different axial positions, giving rise to the irregularity seen in Fig. 4.2(c). By decreasing the sampling time to 80 seconds, or just by taking 150 samples, as well as ensuring that only one particle was used as sample for a given set of complete laser power interval, the uneven data sets could be avoided.

A comparison between the preliminary results and final results are shown in Fig. 4.3. The orange graphs with square points show the preliminary results, while the final results are depicted as purple graphs with diamond points. The final results are the same graphs shown in Fig. 4.1. In the 4 μm-sized particle, it can be seen in Fig. 4.3(a) that the preliminary result was significantly higher and less linear than the final result. The preliminary result values were also inconsistent with other works using the same-sized particle [93]. For the 2 μm-sized particle shown in Fig. 4.3(a), although the measured trapping stiffness values were comparable, the linearity was better for the final result. These comparisons show that the measurement of the positional variance, and in effect, the trapping stiffness estimation, had improved when the problems were resolved using the proposed solutions.

4.3 Cell force measurement

Because the optical trap behaves like a Hookean spring, the force exerted on the cell, or the outside force, is equal to the force from the optical trap. The force

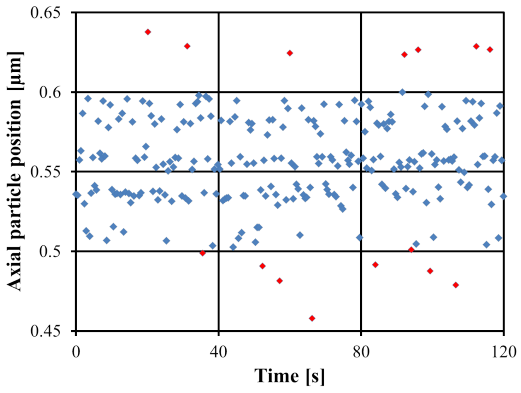

(a)

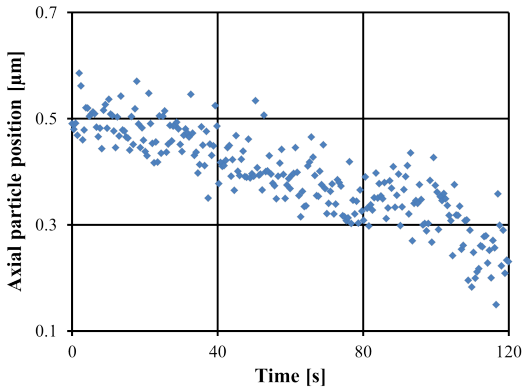

(b)

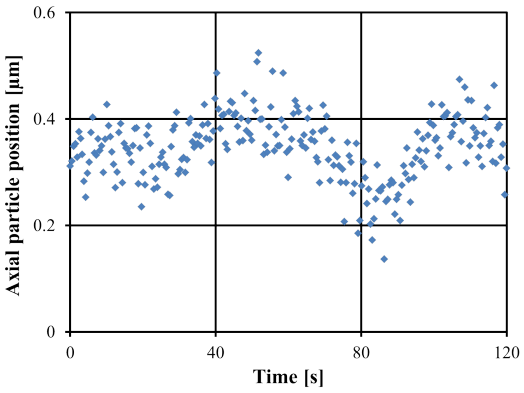

(c)

Figure 4.2: Examples of fluctuating particle data set with (a) spikes (shown in red) of axial particle position for a given laser power, and (b-c)skewed results of axial particle movement.

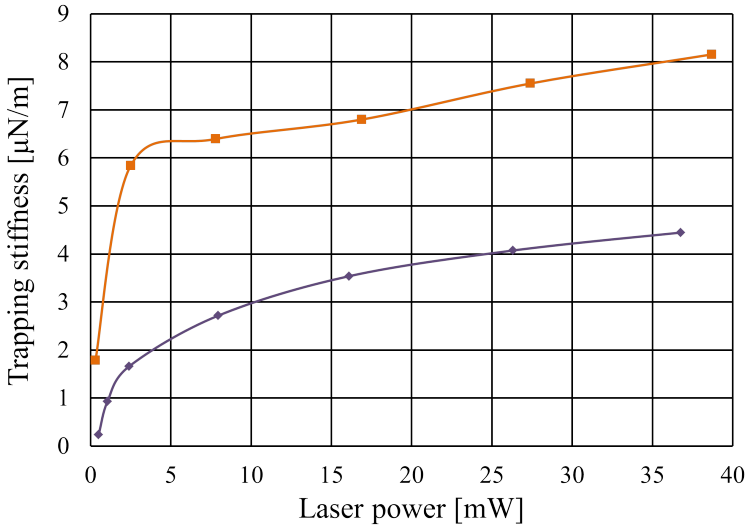

(a) 4 μm-sized particle

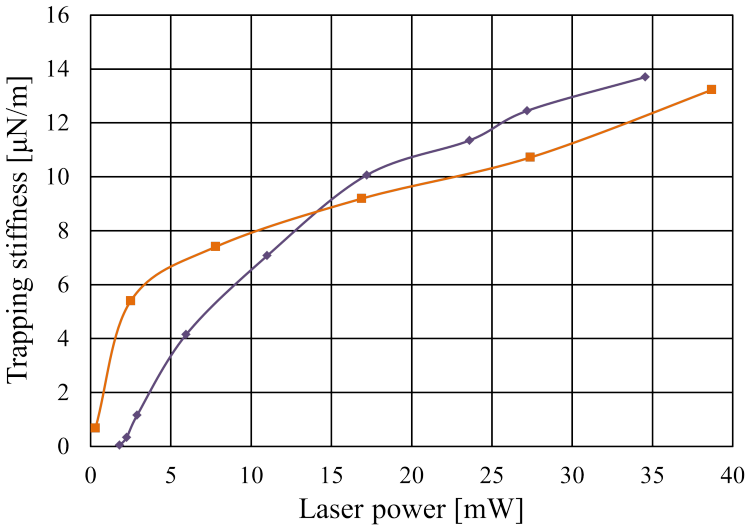

(b) 2 μm-sized particle

Figure 4.3: Comparison of preliminary (orange square points) and final (purple diamond points) trapping stiffness measurements of (a) 4 μm-sized particle and (b) 2 μm-sized particle. The preliminary results exhibit higher estimated trapping stiffness values for the bigger particle, but comparable stiffness values for the smaller particle. Final results show higher linearity of trapping stiffness values as a function of laser power for both particle sizes.

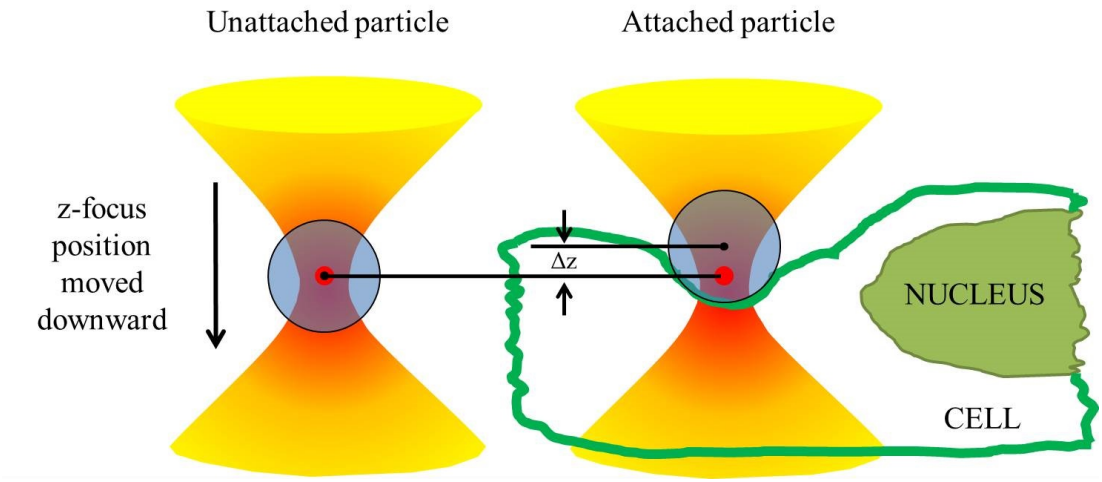

Figure 4.4: The change in axial particle movement of an unattached particle and an attached particle is the estimated Δz. The red dot denotes the focus spot of the laser, while the black dot is the center of the particle. The unattached particle has the particle center and focus spot are in the same position, as oppose to the attached particle when the particle center is not in the equilibrium position.

can then be computed using Hooke's law shown in Eq. 2.4. The trapping stiffness is computed in the previous section, thus the Δz will be estimated in order to determine the exerted force.

The Δz necessary for the cell force measurement is computed as the shift of the particle from the laser focal spot position. When a particle is stably trapped, the particle and the laser spot are in equilibrium, That is, the laser focal position and the center of the particle are approximately in the same position. When the particle is attached on the cell, the particle is hindered by the cell to move further thus there is a change in the axial position between the particle and laser focal position, as shown in Fig. 4.4.

To obtain the Δz, the axial displacements of an unattached particle and an attached particle on the cell were taken. For the 4 μm unattached particle experiments, from an initial position, the lens L1 was set to move 15 mm closer and farther from the microscope, creating an upward and downward motion, respectively, while for the 2 μm unattached particle, the lens L1 was moved 12 mm. For the cell experiments, the same length of lens L1 translation was set for the

respective particles. For example, for the 4 μm-sized particle, the lens L1 was also set to move for 15 mm. The particle was trapped and was also first moved downward as to "push-down" onto the cell, i.e., the cell was probed using the particle for five repetitions at a particular locale. This was to ensure that the particle would form an attachment with the cell. Afterwards, the lens L1 returned to the initial position, and then the particle movement was changed to move upward, and a "pull-up" movement was done.

Since it was necessary to ascertain that the thickness of the cell sample is much greater than the deformation that will be created as specified by the Hertz model assumption, the particles were placed on the surface of the cell less than 4 μm away laterally from the boundary of nucleus. Given that the nucleus is the thickest part of the cell, it was assumed that placing the particles within the boundary of the nucleus would ensure that an appropriate thickness would be established. Sample images are shown in Fig. 4.5 while the graph results are shown in Fig. 4.6.

From the sample images, it was observed that for the unattached particle, the apparent size and shape change was clearly observable. On the other hand, the unattached particles exhibited far less change in apparent size and shape. Although the changes were not visually obvious, the change in particle movement could still be measured as seen in the graph results. It was also seen in the attached participle images that the particles were placed less than 4 μm away laterally from the nucleus.

In Fig. 4.6, mechanical errors, such as drift in objective lens height, and Brownian motion experienced by the unattached particles provided discrepancy from a linear model. Also, as evident in Fig. 4.6(a), the axial position of the 4 μm-sized particle did not correspond to the z-focus position. Errors mainly caused by spherical aberration had possibly influenced the deviation of the particle position displacement from the z-focus position translation. In comparison, the inconsistency was not apparent in the smaller particle as seen in Fig. 4.6(b). The particles attached to the cell exhibited significantly less movements. The downward movement was explained further in the next section. On the other hand, the upward movement showed gradual increase in particle displacement, suggesting that there was particle-to-cell adhesion. To verify the adhesion, after completing

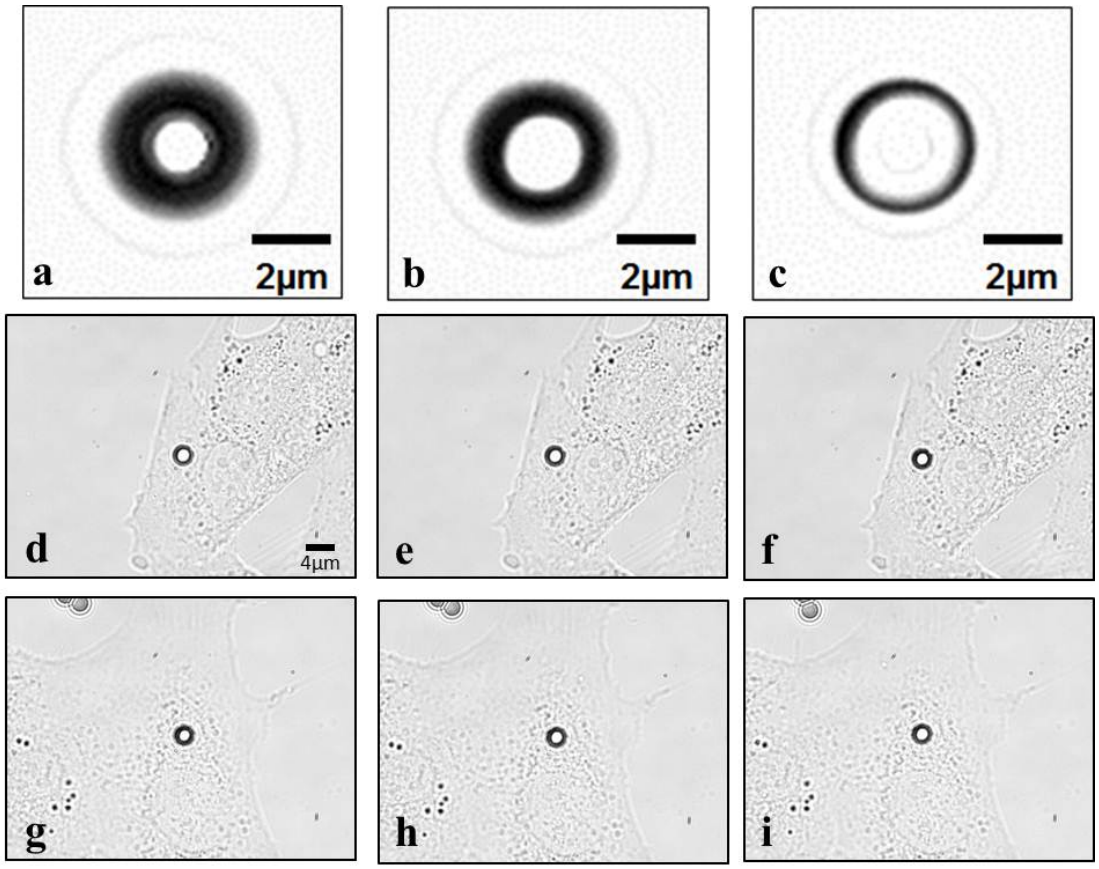

Figure 4.5: Sample images of the 4 μm-sized particle moved in the axial direction at initial lens L1 position or 0 mm position, 7.5 mm lens L1 position, and 150 mm lens L1 position, respectively. a-c) Unattached particle was moved downward. (d-f) attached particle was moved upward, and g-i) attached particle was moved downward.

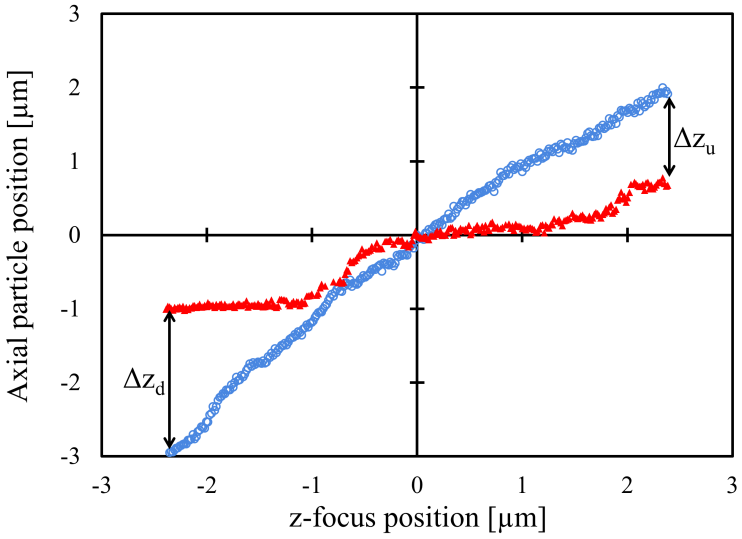

(a) 4 μm-sized particle

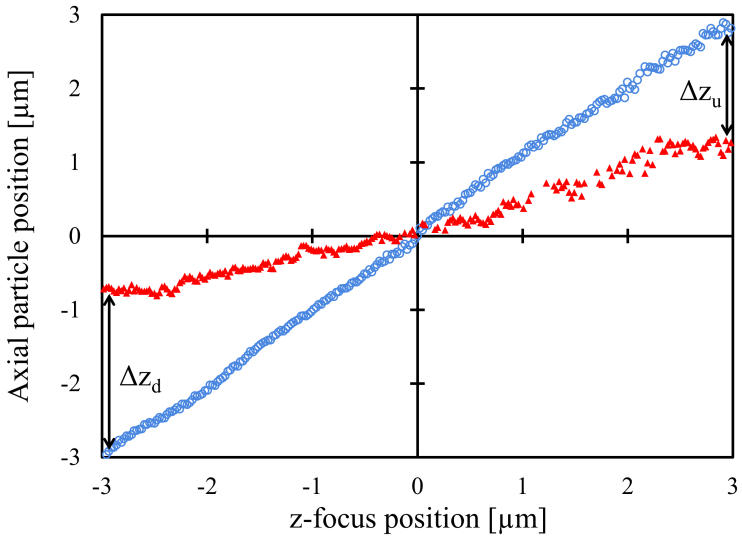

(b) 2 μm-sized particle

Figure 4.6: Results from a single data set for axial displacement of (a) 4 μm-sized particle and (b) 2 μm-sized particle. The attached particle displacement (red line) had significantly less movement compared with the unattached particle displacement (blue line). The Δz was measured as the difference in the unattached particle displacement and attached particle displacement. For the unattached particle, no discernible change in apparent particle size was observed as oppose to the changes in the unattached apparent particle sizes.

a set of upward motion, the trapped particle was moved laterally using the stage. It was observed that the trapped particle moved along with the stage, but the particle springs back towards the cell after some stage translation. It was also noted that tethers were formed between the particle and cell.

Taking the trapping stiffness results mentioned in Section 4.2 and using Eq. 2.4 to compute the forces, the 4 μm-sized particle exerted a downward force of 9 pN and an upward force of 6 pN. the 2 μm-sized particle, on the other hand, exerted a downward force of 25 pN and an upward force of 14 pN.

Force measurement discussion

The main difficulty in the force measurement experiment was obtaining the attached particle movement. The problem comes in two parts, first: the cell posed an inhomogeneous background. As observed from Fig. 4.5(a-c), the background was homogeneous or had uniform color composition for the unattached particle. The edge of the particle could be clearly distinguished and the image analysis program could detect the changes in apparent particle size with more linearity. If the particle is placed on the cell surface as in Fig. 4.5(d-i), the particle edge became uneven. This caused the image analysis program to detect noisy signals, albeit the apparent particle size did change as the particle was moved downward or upward. This problem was solved by adjusting the image analysis program and lighting conditions. The apparent particle sizes were rechecked and recalibrated to make the data as precise as possible. Offsets were also introduced in the graphs to align the initial particle position and z-focus position.

The second part of the problem was the cell location. In connection to this, the number of particle motions per motion set also caused a problem. Initially, Fig. 4.7 shows the graph of an uncoated 4 μm particle probing the edge of the cell for at least ten repetitions. In this case, the shape of the graph changed over repetition. For one, the first few data that were acquired showed that at 0.5 μm downward particle movement, the particle was hindered by the cell to go down further. This suggested that the particle had reached the cell surface. As more probing were done, the particle movement became as high as 2 μm. The change in graph results per repetition showed that as the cell was probed further at the same cell locale, the cell might have been strained, such that it got flattened.

This explains the increase in particle movement in the downward direction. It was also assumed that in the 0.5 μm particle movement in the initial probing, the particle had not touched the cell yet because as more probing experiments were done, a linear particle movement could be observed. Although this preliminary experiment showed a gradual breakdown of the cell, it did not provide the cell force information because the average of attached particle movement was almost equal to the cell thickness. Not to mention, repetitive probing in one cell locale also disobey one of the Hertz model assumption that the sample is elastic in nature. Another problem with probing the edge of the cell was that no clear cell deformation could be established. This was because the cell membrane farther from the nucleus are softer and thinner, making these locations difficult to measure the elastic constant. Thus the cell attachment experiments were conducted at the location near the nucleus boundary. The repetitions per cell location were also decreased to five repetitions. With the collagen coated particles, particle-to-cell adhesion can occur at less than a minute. Since each downward motion is conducted in 80 seconds, adhesion was surely established. The decrease in repetitions however caused a problem in terms of usable data. In this case, the solution was to increase the number of experiments.

4.4 Cell stiffness measurement

In this dissertation, the measurement of the cell stiffness using the Hertz model equation is demonstrated. Based on Eq. 2.5, obtaining the localized cell stiffness is a matter of computing the constant, $\frac{E}{(1-\nu^2)}$. The radii of the particles are known, while the deformation is performed during axial cell probing, and subsequently measured. Lastly, the force of the particle is computed using the Hookes law as discussed in the previous section, wherein the trapping stiffness was also computed. Measurement of cell deformation and cell stiffness will be explained in this section.

For the computation of cell stiffness, only the results for the downward motions are taken into account. In the cell experiment image in Fig. 4.5, the initial lens L1 position was the same for the three sets of experiment (Refer to Fig. 4.5(a, d and f). But the change in apparent particle size for the attached particles,

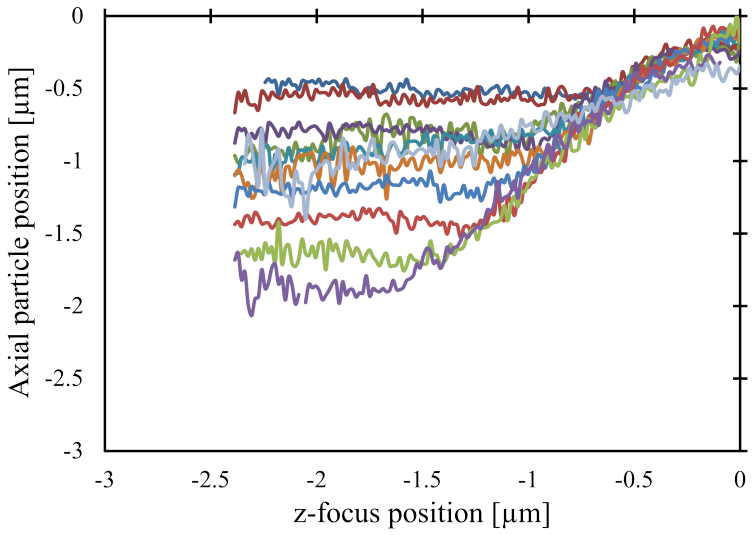

Figure 4.7: Sample images of the 4 μm-sized particle attached and pushed downward on the edge of a cell.

Fig. 4.5(d-f) and Fig. 4.5(g-i) were not distinguishable. These figures show that the particle movement was very limited because the particles were attached to the cell. The attached particle images also showed how close the particles were on the cell nucleus. Because the nucleus is the thickest part of the cell, the surrounding area of the nucleus are reasonable thick so that the deformation made (on the particular cell locale) will be significantly smaller than the cell thickness.

The cell deformation δ estimation is as follows: a magnified version of the graph results from the previous section is shown in Fig. 4.8. A particle was manually placed above the cell surface. From the initial z-focus position, the particle was moved downward until it attached to the cell surface at point 1, but no deformation was formed yet. From point 1, as the optical trap went further down, force was applied on the cell thus creating the deformation. The graph was seen as having little change in the movement until point 2, at which the axial particle displacement became stable. The cell deformation was then estimated as the change in axial particle position from point 1 to point 2. The deformations were computed as 350 nm and 500 nm for the cell probed using 4 μm- and 2 μm-sized particles, respectively.

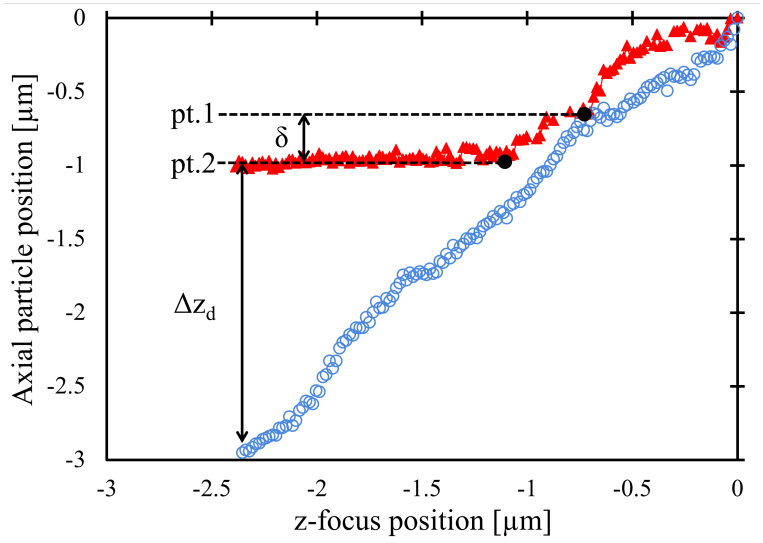

(a) 4micron

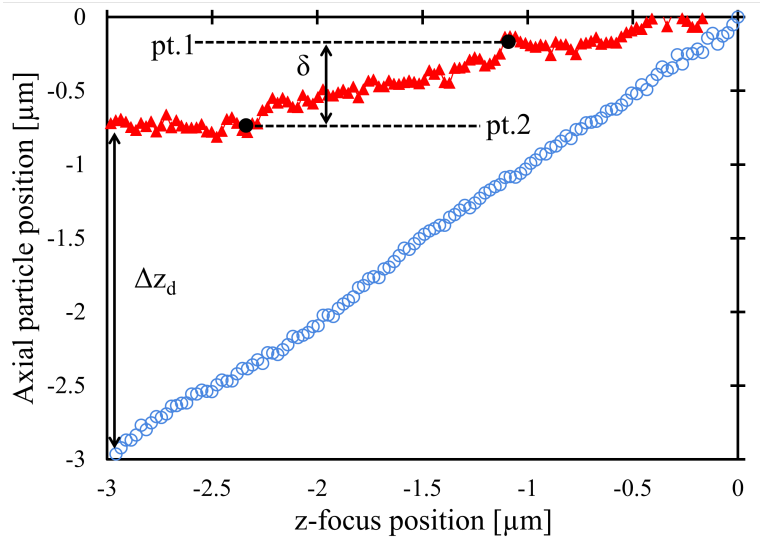

(b) 2micron

Figure 4.8: Results from a single data set for axial displacement of (a) 4 μm-sized particle and (b) 2 μm-sized particle. For the cell stiffness measurement, the downward motion was examined. The cell deformation δ was estimated from pt. 1 to pt. 2.

Based on the experimental procedure, it was predicted that the attached particle would have similar positions with the unattached particle from the initial position up to point 1. This was because no particle-to-cell attachment was expected. However, based on the results, the attached particle had exhibited small movements. These movements could be caused by the cell membrane and even by components external from the cell itself. In eukaryotic cells except RBCs, the cell membrane is very soft and is often neglected in cell stiffness measurement. It is the cytoskeleton that provides the cellular mechanical properties. Hertz model dictates that the sample is homogeneous, isotropic, and infinitely thick, however, these assumptions do not necessarily apply to cells. Nevertheless, the mechanical behaviour of cells often closely follow the Hertz model prediction [125]. In the results, the deformation was estimated when the attached particle had reached point 1 since from this point up to point 2, the gradient of particle movement changed as compared with the gradient formed from initial position up to point 1. The probing of the stiffer cytoskeleton was assumed to have began at this point. Finally, from point 2 until the end of z-focus position, the particle movements became stable suggesting the cell locale could not be probed further.

Now that the exerted forces, radii of particles, and deformations were taken into account, localized Balb3T3 cell stiffness was computed using Eq.2.5, with Poisson's ratio assumed to be 0.5 for soft biological materials [126]. The cell stiffness results were 17 Pa and 40 Pa for the cell probed using 4 μm- and 2 μm-sized particles, respectively.

The difference in the cell stiffness measurements were expected from the different probed cell locales and different cell samples. Because the cell structure is composed of different materials, it was expected that the mechanical behaviour would also yield varying results. Given that the particles were situated within a range from the nucleus, the elastic modulus estimated over the region bounded by the smaller contact area resulted in greater value. The exerted force was also greater for the 2 μm-sized particle, and the deformation made was slightly larger than with the deformation made using the 4 μm-sized particle.

Cell stiffness measurement discussion

The experimental method was similar to using atomic force microscopy (AFM) in terms of creating deformations. However, in AFM, an NIH 3T3 cell has an estimated cell stiffness measurement of 1 to 2 kPa [67]. These values are valid since the typical stiffness values of animal cells vary from 100 Pa to more than 10 kPa, with loading forces ranging from 100 pN to 1 nN [56]. However, the first concern was that the results shown in this dissertation were comparatively small compared to the AFM results. The difference in the computed localized cell stiffness using optical tweezers and AFM was found in the measured force: one of the advantages of using optical tweezers is the range of forces that it can measure is the lower range: 0.1 to 100 pN; whereas AFM can measure 10 to 10^4 pN and above [6]. Since the same amount of axial cell deformation can be done by both AFM and optical tweezers, and a particle with equal radius can be used, it is expected that the cell stiffness result will only be affected by the force exerted by the particle. Comparing the measured localized cell stiffness with other optical tweezers methodology, traditionally, optical tweezers are used to attach particles on the cell and are moved laterally. The cell stiffness of RBC is also computed using different models wherein the results vary from 2.5 $^{\mu N}/_{m}$ to 200 $^{\mu N}/_{m}$ [22,127]. The large range of cell stiffness measurement in both AFM and laterally manipulated optical tweezers experiments is due to using different samples, and probing different locales, and using different measurement models, and methods, to name a few specific environments. Other results of cell stiffness at different locales are shown in Fig. 4.9 and Fig. 4.10 using 4 μm- and 2 μm-sized particle probes, respectively. For the 4 μm-sized particle examples, the deformations created were 300 nm and 250 nm, with exerted force computed as 9.5 pN for both data sets. The localized cell stiffness measurements were 23 Pa and 30 Pa, respectively. In the bigger particle, the results were comparable. For the 2 μm-sized particle, the deformations created in the supplementary examples were smaller, 200 nm as oppose to 500 nm of the given result. With exerted forces at 26 pN and 29 pN, which were also comparable with the 25 pN force reported in the results, the localized cell stiffness measurements were significantly higher in the supplementary examples with 164 Pa and 182 Pa. Referring to the supplementary results for the smaller particle, it was observed that the downward movement of the attached

2 μm-size particle were less apparent. That is, point 1, which was the point of contact between particle and cell, was more difficult to determine. The higher computed localized cell stiffness values using the smaller particle provided measurements that are within the range of cell stiffness values obtained using AFM. However, these values are still in the lower range, which still offers the advantage of how optical traps can exert smaller forces, and subsequently measure smaller localized cell stiffness values, than AFMs. The thrust of this dissertation is to offer a new approach: using an axial optical tweezers, probing a cell similarly to how AFM experiments are conducted, and using the Hertz model equation, it is feasible to measure the localized cell stiffness quantitatively.

4.5 Discussion

This section summarizes the problems encountered during the application of the axial manipulation system in measuring the localized cell stiffness. Other matters that directly affect the cell stiffness measurement are also mentioned here. Further details are included in the respective sections, the trapping stiffness in Section 4.2, force measurement is in Section 4.3, and cell stiffness measurement in the previous section.

The trapping stiffness should have a linear relationship with respect to laser power [102]. In Fig. 4.1, it was observed that the trapping stiffness became saturated even before the laser power reached 10 mW. This saturation rose from the decreasing trapped particle displacements at increasing laser power, which can be seen at the sudden stabilization of particle movement at the mentioned laser power in Fig. 4.1(a). Since trapping stiffness provides the information on how stable the optical trap is, and directly affects the cell force measurement, proper calibration and measurement of the axial particle displacement are vital. The small deviation in the particle position can affect the overall computation of the variance, especially when using the equipartition theorem method as discussed in 2.4. The problems in fluctuating particle movement, such as the spikes and skewed data shown in Fig. 4.2, can also be resolved by ideally using one particle as sample for a given data set, and decreasing the data acquisition duration from 120 seconds to 80 seconds. Especially for the 2 μm-sized particle, the CCD camera

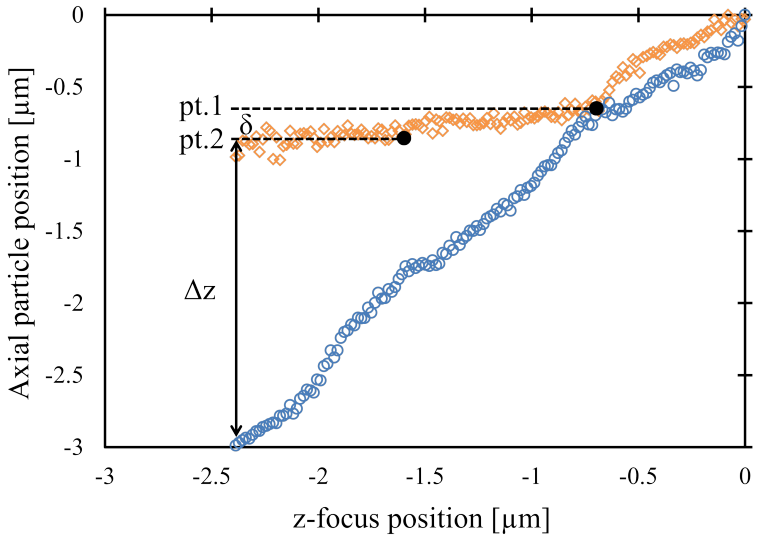

(a)

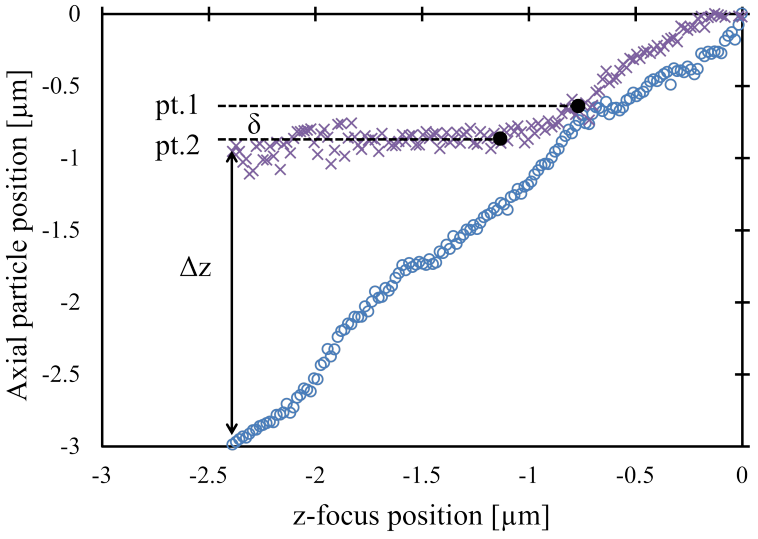

(b)

Figure 4.9: Supplementary results from single data sets for localized cell stiffness measurement using 4 μm-sized particle as probe.

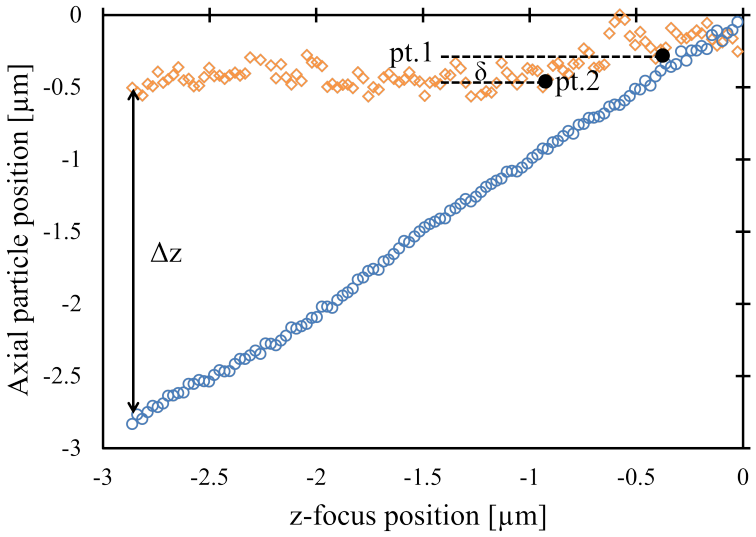

(a)

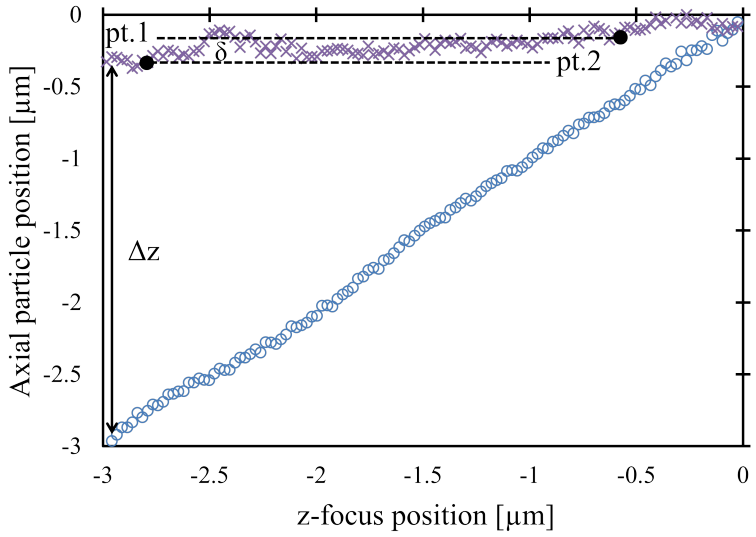

(b)

Figure 4.10: Supplementary results from single data sets for localized cell stiffness measurement using 2 μm-sized particle as probe.

shutter speed was increased from 3 ms to 1 ms, thus taking in more frames to track the fast movement. The relay lens also improved the procurement of particle movement.

With the same length of z-focus translation, the linear regions in both the upward and downward displacements of trapped particles were determined. However, the motion was divided into two, that is, from an initial position, the lens L1 was moved closer to the microscope, enabling the optical trap to move downward. After that motion, the lens L1 will return to the initial motion, and then the lens L1 will be moved farther from the microscope to move the optical trap upward. Although the lens L1 was set to move for a given length for both the upward and downward motion, the length of axial particle movement was not the same for the upward and downward motions, as seen in Fig. 4.6. The difference in the upward and downward graphs of the unattached particle displacement might be due to spherical aberrations, and mechanical errors as explained in Section 3. On the other hand, difficulty in the cell experiments was primarily caused by the distortion of particle movement due to repeated cell probing. The cell location and number of push-down/ pull-up repetitions affected the estimation of Δz, as well as the deformation δ for the cell stiffness. The repetition was changed to 5 per cell locale, and instead of probing the edge of the cell, the particle was placed near the nucleus boundary. The decreased number of repetition lessened the probability of flattening the cell surface, but still ensured particle-to-cell adhesion. The area near the nucleus provided a thicker and stiffer background, thus δ could be observed. Finally, the image analysis program compensated for the errors caused by changing contrast, especially for the darker background from the cell and medium.

Finally, for the measurement of cell stiffness, it is believed that there had yet any literature which suggests that the localized cell stiffness can be measured by an optical trap that is manipulated in the axial direction. The sample preparation and experiments are also simpler when using optical tweezers as oppose to using AFM. In AFM, more considerations, such as sample mounting, and loading, as well as setting up the cantilever, laser, and position detector, are tackled. As oppose to optical tweezers, in which the setup consists of mounting the sample on the microscope, aligning the laser, and setting the CCD camera to obtain

the images. The accuracy of localized cell stiffness measurement cannot be be determined since there has yet to be a standard for the measured values of cell stiffness given that cells have different components in particular locales. The reproducibility of the proposed system can be improved by ensuring that the probed cell locales are within the same area. It was observed that the estimated deformation can significantly affect the computed localized cell stiffness. In the future, the experiments can be patterned according to AFM wherein the force curves will be compared between a cell sample and a stiff substrate such as glass slide. Further measurements of localized cell stiffness wherein the two different-sized particles are placed closely to each other may offer more information regarding the effects of smaller probes in localized cell stiffness. Application on elasticity mapping of cells [126, 128] using optical tweezers can also reveal insights on the different mechanical characteristics of cell locations, such as the cytoskeleton, or cell cortex. Incorporating other image microscopy techniques with the elasticity mapping may also elucidate which specific protein or cell components are activated when the cell is mechanically stimulated from an external source.

4.6 Chapter summary

The application of the axial manipulation system (see Section 3) to localized cell stiffness measurement was discussed in detail. The purpose of this chapter included the discussion of the measurement and estimation of the different parameters necessary to measure the elastic constant of a cell using Hertz model equation. The measured results are enumerated in Table 4.1. The summary per experiments are as follows:

1. **To measure the trapping stiffness**

   Equipartition theorem was used in measuring the trapping stiffness of a 4 μm- and a 2 μm-sized particle. Eq. 2.3 computes the trapping stiffness, wherein the variance of the trapped particle movement is the only parameter that must be measured. Fig. 4.1(a) shows the standard deviation of the trapped particle at different laser power. At laser power less than 10 mW, the particle movement was large. At more than 10 mW, the particle movement stabilized. Since variance is the square of standard deviation,

Table 4.1: Summary of estimated parameters used for computing the localized cell stiffness

	4μm-sized particle				**2μm-sized particle**			
	Down		**Up**		**Down**		**Up**	
	Attach	**Unattach**	**Attach**	**Unattach**	**Attach**	**Unattach**	**Attach**	**Unattach**
lens L1 translation [mm]	15				12			
Axial movement [μm]	1	3	0.7	2	0.7	3	1.3	3
Δz (μm)	1.4		2.35		4.08		2.99	
Trapping stiffness [μN/m]	4.5				11.4			
Computed force [pN]	9		6		25		14	
Cell deformation [nm]	350		N/A		500		N/A	
Cell stiffness [Pa]	17		N/A		40		N/A	

equipartition method is a biased estimator. In this case, proper filtering of particle movement data is necessary. Fig. 4.1 shows the measured trapping stiffness as a function of laser power. The particle movements stabilized at different laser powers. The 4 μm-sized particle stabilized at laser power equals 36.8 mW, with computed trapping stiffness of 4.5 $^{\mu\mathrm{N}}/_{\mathrm{m}}$. On the other hand, the 2 μm-sized particle stabilized at 23.6 mW with trapping stiffness of 11.4 $^{\mu\mathrm{N}}/_{\mathrm{m}}$.

2. **To measure the force exerted on the cell using a particle as probe**

   After computing the trapping stiffness, the force was computed using Hooke's law, Eq. 2.4, where Δz is the shift of the particle from the equilibrium position. The equilibrium position of the optical trap was estimated as the maximum position of an unattached particle for a given z-focus position. The particle was then attached to a cell and provided a change in the maximum particle movement. The difference in the movement of an unattached particle and an attached particle provided the estimation of Δz. This estimation was discussed in Section 4.3. Differences in axial movements for the upward and downward motions, and in effect in Δz, were computed. For the 4 μm-sized particle, the downward and upward forces were 9 pN and 6 pN, respectively. While for the 2 μm-sized particle, the computed downward and upward forces were 25 pN and 14 pN, respectively. Specific cell probing locations and repetitive experimental motions provided the difficulty in this experiment.

3. **To measure the cell stiffness of a Balb 3T3 cell**

   In measuring the cell stiffness, only the downward motion, or push-down action, was considered. Eq. 2.5 describes the relationship of exerted force and cell deformation δ, wherein the cell stiffness can be computed from the elastic constant, $\dfrac{E}{(1-\nu^2)}$. Most of the terms were already computed at this point, and the constant ν was established. The remaining parameter δ was then described in Section 4.4. The deformation was performed on the cell surface close to the boundary of the nucleus. The stiff material provided the information of particle contact on the cell surface, the subsequent cell deformation, until the point where the particle can no longer be pushed

down further. Finally, the cell stiffness was computed using the Hertz model equation, which had not been utilized before for the measurement of localized cell stiffness using optical tweezers. The localized cell stiffness resulted to 17 Pa and 40 Pa for the 4 μm- and 2 μm-sized particles, respectively.

The proposed axial manipulation system provides an alternative method from using AFM as the source of external axial force. The Hertz model equation is also a different approach for optical tweezers experiments in computing the localized cell stiffness. The results provide an insight on the cell reaction to small forces exerted by optical tweezers.

The next chapter concludes the dissertation. Important points about the proposed axial manipulation system and its application to localized cell stiffness measurement will be reviewed. Finally, the implications of the proposed method in the study of nanomanipulation in cell mechanics and single-molecule force spectroscopy will be discussed.

Chapter 5

Conclusion

The mechanical properties of cells provide insights about the cell structure and cellular components. The different biological components can be mechanically stimulated, thus reveal information about the cellular components' roles in motility, adhesion, and division, to name a few functions. Being able to exert small forces in specific cell locales can also show the important roles of actin filaments and microtubules in transferring signals to the whole cell. Some of the viable applications of measurement of mechanical properties of cells include stem cell and cancer research. Nano-surgery also necessitates the knowledge of cell stiffness and viscosity, whereas medical diagnostics and cell regeneration studies can use these mechanical properties as disease indicators and to improve drug delivery. Cell mechanics and single-molecule force spectroscopy are two areas that deals with the study of cellular reaction to outside forces. The cell palpation system (CPS) is an existing method that measures the membrane support stiffness during focal adhesion using Eq. 2.2, which describes the motion equation of the particle. CPS uses an optical tweezers that can manipulate the particle in the lateral direction. From this work, further studies were realized: (1) since cells inherently move in three dimensions, in order to obtain a broader understanding of the cell structure, it is proposed that an axial movement will be incorporated in the CPS. However, given the completed CPS, (2) this posed a limitation in terms of customizing the optical tweezers setup. And (3), there is need to find a suitable method of measuring the cell stiffness with an axially manipulated optical trap serving as the source of the outside mechanical stimulus. This dissertation had served to

provide a solution to these three problems.

5.1 Proposed axial manipulation system

A simple yet sensitive optical tweezers scheme was proposed wherein the focus of the laser was axially manipulated using motorized lens. Changing the divergence of the laser beam moved the laser focus upward or downward along the optical axis. Polystyrene particles with different sizes were used to test the change in axial laser position. In order to measure the axial particle movement, the defocused particle images were taken using a CCD camera per lens L1 step, and the camera and lens translation were controlled using a computer program. This setup provided detailed view on the change in apparent particle size. An image analysis program was also developed to precisely measure the change in apparent particle size. A calibration graph was created to provide a relationship between axial position and apparent particle size. Then the z-focus position was taken from the gradient of axial particle movement with respect to lens translation. For the experiments, the initial lens position was investigated that could provide linear relationships between the z-focus position and axial particle position. The two different-sized particles also served as comparison for the effect of particle size when moved with the same length of laser focus. The 4 μm-sized particle provided at least 5 μm particle movement until the estimated particle position became ambiguous. This ambiguity stemmed from the assumption that the apparent particle size as having a linear relationship with axial movement. In the case of the 2 μm-sized particle, a maximum of 12 μm particle movement was obtained. The graphs from different initial lens position did not result in ambiguity. From these results, the linear regions for both particles are observed, as well as reveal the considerations that will be necessary for the subsequent experiment on biological materials.

5.2 Localized cell stiffness measurement

Using the proposed axial manipulation system, a Balb3T3 cell was probed using 4 μm- and 2 μm-sized particles. The probing experiment was reminiscent of

atomic force microscopy method thus the Hertz model equation was used as the means to compute the localized cell stiffness. Eq. 2.5 necessitates the knowledge of probe radii, deformation created on the cell, and measurement of force exerted by the particle. The force was measured using Hooke's law, in which the trapping stiffness of the optical tweezers was measured using equipartition theorem. The Δz, which is the shift from the equilibrium position of the trap, was estimated as the difference in the attached and unattached particle movement. The trapping stiffness measured were 4.5 $^{\mu\mathrm{N}}/_{\mathrm{m}}$ and 11.4 $^{\mu\mathrm{N}}/_{\mathrm{m}}$ for the 4 μm- and the 2 μm-sized particle, respectively. The Δz for the upward and downward particle motions were also computed. The 4 μm-sized particle had computed forces of 9 pN and 6 pN for the downward and upward motions, respectively. On the other hand, the 2 μm-sized particle had computed forces of 25 pN and 14 pN for the downward and upward motions, respectively. Cell deformations created near the boundary of the nucleus were estimated as 350 nm and 500 nm for the 4 μm- and the 2 μm-sized particle, respectively, resulting to localized cell stiffness measurements of 17 Pa and 40 Pa.

5.3 Future work

Further work can be done for the computation of the pull-up cell stiffness, where the surface energy of both the attached particle and cell will be considered. Comparing the stiffness of healthy and unhealthy cells, and elasticity cell mapping are also possible applications for the proposed system. Integrating the axial manipulation system into the CPS, in which the control for the galvano-mirror and lens translation are included in a single program, can improve the ease of use of the system. This development can also include the image analysis program within the same program thus creating a three-dimensional optical tweezers system. The problem with the discrepancy of z-focus position movement and axial particle position movement can also be tackled, including the improvement of precision in terms of detecting the fast movement of the fluctuating particles in the trapping stiffness experiment.

Acknowledgements

First of all, I would like to thank my previous and current supervisors, Professor Kotaro Minato and Professor Shigehiko Kanaya for their continuing support. I am overwhelmed by their generosity and graciousness in helping me achieve my goals even beyond NAIST. I am very grateful that you have given me the opportunity to be part of your laboratories.

To Associate Professor Tadao Sugiura, I cannot express how thankful I am that I was accepted under your supervision. Sugiura sensei, you are truly an inspiration. Even at my lowest, you were always guiding me. Your patience and never-ending advices shaped up my work, and without your motivation, I do not think I will be able to accomplish as much. I will always remember your teachings and kindness to all of us, and I will always strive to do my best.

I would like to thank my thesis committee, Professor Shigehiko Kanaya, Professor Tsukasa Ogasawara, and Associate Professor Tadao Sugiura for your kind advices and helpful comments for the improvement of this dissertation. Your invaluable questions, especially during my midterm and public defense presentation, are highly appreciated.

Thank you to Panasonic scholarship for trusting in me and supporting me. I always know that I will see everyone again. To the past and present Panasonic scholarship staff, I will always be available to support you, as you support me even after the end of my program.

Thank you to all members and staff of Biomedical Imaging and Informatics Laboratory, past and present, which is now called Computational Systems Biology Laboratory. In my stay here in the laboratory, I do not remember ever being lonely or homesick. My Japanese learning abilities improved gradually because of everyone's kind talks and funny stories. To Assistant Professor Tetsuo Sato,

thank you very much for the support, stories, and patient reminders. To the Optics group, I will always remember everyone with fond memories. To my favourite seat mate, see you in Malaysia! Ohashi san, thank you very much for your patience and kind greetings.

To the staff of the administrative building, in particular the Student Affairs Division. My NAIST transition was made brighter and easier because of your kindness and understanding, not only to me but, to all of the foreign students. Whenever I come for a visit in the future, I will surely drop by for a chat. Thank you very much for all the assistance and support you have given me.

To my friends in and outside of NAIST. Some have gone home or went to other countries, and some are still here in Japan. YMCA friends, Panasonic friends, NAIST friends. I will particularly treasure the NAIST Bubble series. I hope everyone will have a thing or two to include in those stories, and please share them to me! Hi, Mare!

Nais kong magpasalamat kay Emarc Magtanong *para sa araw-araw.* Thank you for printing and making the hard bound copies of my dissertation.

To my family, thank you for the support and encouragement. Although I am away, it still feels like I am there with you guys every time you say hello to me. To Mr. Selwyn N. Dy and Mrs. Zenaida C. Dy, thank you very much for your love and understanding. With your constant talks and casual messages, being away from home became bearable. I know it is not much compared to everything you have given me, but this is for you. I will always do my best to be a *mabuting anak*.

"In our weakness and vulnerability, bless us with your grace to soar beyond limits. ad majorem Dei gloriam."

Publication List

Journal

1. Mary-Clare Dy, Shigehiko Kanaya and Tadao Sugiura. Localized cell stiffness measurement using axial movement of an optically-trapped microparticle. In *Journal of Biomedical Optics*. vol.18 no.11 (To appear). [Corresponds to Chapters 3 and 4]

International Conferences

1. Mary-Clare Dy, Tadao Sugiura and Kotaro Minato. Axial displacement and position measurement of single particle using optical tweezers. In *Proceeding of Biomedical Optics, OSA Technical Digest (Optical Society of America).* Poster presentation, paper BSu3A.1. Miami, Florida, April 2012. [Corresponds to Chapter 3]

2. Mary-Clare Dy, Tadao Sugiura and Kotaro Minato. Investigation of the mechanical property of individual cell using axial optical tweezers. In *Proceedings of SPIE 8587, Imaging, Manipulation, and Analysis of Biomolecules, Cells, and Tissues XI.* Poster presentation, p. 85871U. San Francisco, California, February 2013. [Corresponds to Chapter 3 until Chapter 4.3]

Domestic Conferences and Meetings

1. Mary-Clare Dy, Shigehiko Kanaya and Sugiura Tadao. Axial cell-force measurement using optical tweezers. In *Information Photonics Research Group Meeting, Japan Society of Applied Physics,*. Tokyo-Japan. June 2013.

2. Mary-Clare Dy, Tadao Sugiura and Kotaro Minato. Axial manipulation of particle and investigation of mechanical property of individual cell using optical tweezers. In *Optics and Photonics Japan Conference 2012*. Tokyo-Japan. October 2012.

3. Mary-Clare Dy, Tadao Sugiura and Kotaro Minato. Axial particle displacement using optical tweezers. In *JSAP-OSA Joint Symposia (73rd JSAP Autumn Meeting), Japan Society of Applied Physics,*. Ehime-Japan. September 2012.

4. Mary-Clare Dy, Tadao Sugiura and Kotaro Minato. Axial displacement and position measurement of single particle in optical tweezers. In *Information Photonics Research Group Meeting, Japan Society of Applied Physics*. Osaka-Japan. June 2012.

5. Mary-Clare Dy, Tadao Sugiura and Kotaro Minato. Axial displacement and position measurement of single particle in optical tweezers. In *Optics and Photonics Japan Conference 2011*. Osaka-Japan. November 2011.

References

[1] M. R. K. Mofrad and R. D. Kamm. *Cytoskeletal Mechanics: Models and Measurements in Cell Mechanics*. Cambridge University Press, 2006.

[2] M. P. Sheetz, D. P. Felsenfeld, and C. G. Galbraith. Cell migration: regulation of force on extracellular-matrix-integrin complexes. *Trends in cell biology*, 8(2):51–54, 1998.

[3] R. D. González-Cruz, V. C. Fonseca, and E. M. Darling. Cellular mechanical properties reflect the differentiation potential of adipose-derived mesenchymal stem cells. *Proceedings of the National Academy of Sciences*, 109(24):E1523–E1529, 2012.

[4] S. Puttini, M. Lekka, O. M. Dorchies, D. Saugy, T. Incitti, U. T. Ruegg, I. Bozzoni, A. J. Kulik, and N. Mermod. Gene-mediated restoration of normal myofiber elasticity in dystrophic muscles. *Molecular Therapy*, 17(1):19–25, 2008.

[5] A. Ashkin, J. M. Dziedzic, J. E. Bjorkholm, and S. Chu. Observation of a single-beam gradient force optical trap for dielectric particles. *Optics letters*, 11(5):288–290, 1986.

[6] K. C. Neuman and A. Nagy. Single-molecule force spectroscopy: optical tweezers, magnetic tweezers and atomic force microscopy. *Nature methods*, 5(6):491–505, 2008.

[7] H. Miyoshi, T. Sugiura, and K. Minato. Cell palpation system based on a force measurement by optical tweezers for investigation of local mechanical properties of a cell membrane. *Japanese Journal of Applied Physics*, 48(12):0223, 2009.

[8] J. W. Shaevitz. A practical guide to optical trapping. *Retrieved Jul*, 30:2010, 2006.

[9] T. Ota, T. Sugiura, S. Kawata, M. J. Booth, M. A. A. Neil, R. Juškaitis, and T. Wilson. Enhancement of laser trapping force by spherical aberration correction using a deformable mirror. *Japanese Journal of Applied Physics*, 42(6):L701–L703, 2003.

[10] J. Garcia-Sucerquia, W. Xu, S. K. Jericho, P. Klages, M. H. Jericho, and H. J. Kreuzer. Digital in-line holographic microscopy. *Applied optics*, 45(5):836–850, 2006.

[11] T. Sugiura, M. Nakao, T. Sato, and K. Minato. Nanomanipulation and nanotechnology for future diagnostics. *eHealth: combining health telematics, telemedicine, biomedical engineering, and bioinformatics to the edge: global experts summit textbook*, 134:135, 2008.

[12] J. Dai and M. P. Sheetz. Membrane tether formation from blebbing cells. *Biophysical journal*, 77(6):3363–3370, 1999.

[13] D. E. Ingber. Tensegrity ii. how structural networks influence cellular information processing networks. *Journal of Cell Science*, 116(8):1397–1408, 2003.

[14] A. van de Stolpe, K. Pantel, S. Sleijfer, L. W. Terstappen, and J. M. J. den Toonder. Circulating tumor cell isolation and diagnostics: toward routine clinical use. *Cancer research*, 71(18):5955–5960, 2011.

[15] E. Pierstorff and D. Ho. Monitoring, diagnostic, and therapeutic technologies for nanoscale medicine. *Journal of Nanoscience and Nanotechnology*, 7(9):2949–2968, 2007.

[16] W. Petrich. Mid-infrared and raman spectroscopy for medical diagnostics. *Applied Spectroscopy Reviews*, 36(2-3):181–237, 2001.

[17] I. Dulińska, M. Targosz, W. Strojny, M. Lekka, P. Czuba, W. Balwierz, and M. Szymoński. Stiffness of normal and pathological erythrocytes studied by means of atomic force microscopy. *Journal of biochemical and biophysical methods*, 66(1):1–11, 2006.

[18] D. L. Butler, N. Juncosa-Melvin, G. P. Boivin, M. T. Galloway, J. T. Shearn, C. Gooch, and H. Awad. Functional tissue engineering for tendon repair: A multidisciplinary strategy using mesenchymal stem cells, bioscaffolds, and mechanical stimulation. *Journal of Orthopaedic Research*, 26(1):1–9, 2008.

[19] D. E. Discher, P. Janmey, and Y. L. Wang. Tissue cells feel and respond to the stiffness of their substrate. *Science*, 310(5751):1139–1143, 2005.

[20] S. Suresh. Biomechanics and biophysics of cancer cells. *Acta Materialia*, 55(12):3989–4014, 2007.

[21] V. Swaminathan, K. Mythreye, E. T. O'Brien, A. Berchuck, G. C. Blobe, and R. Superfine. Mechanical stiffness grades metastatic potential in patient tumor cells and in cancer cell lines. *Cancer research*, 71(15):5075–5080, 2011.

[22] J. Sleep, D. Wilson, R. Simmons, and W. Gratzer. Elasticity of the red cell membrane and its relation to hemolytic disorders: an optical tweezers study. *Biophysical journal*, 77(6):3085–3095, 1999.

[23] F. M. Fazal and S. M. Block. Optical tweezers study life under tension. *Nature photonics*, 5(6):318–321, 2011.

[24] M. Allioux-Guérin, D. Icard-Arcizet, C. Durieux, S. Hénon, F. Gallet, J. C. Mevel, M. J. Masse, M. Tramier, and M. Coppey-Moisan. Spatiotemporal analysis of cell response to a rigidity gradient: a quantitative study using multiple optical tweezers. *Biophysical journal*, 96(1):238–247, 2009.

[25] C. O. Mejean, A. W. Schaefer, E. A. Millman, P. Forscher, and E. R. Dufresne. Multiplexed force measurements on live cells with holographic optical tweezers. *Optics express*, 17(8):6209–6217, 2009.

[26] T. A. Nieminen, G. Knöner, N. R. Heckenberg, and H. Rubinsztein-Dunlop. Physics of optical tweezers. *Methods in cell biology*, 82:207–236, 2007.

[27] M. Dao, C. T. Lim, and S. Suresh. Mechanics of the human red blood cell deformed by optical tweezers. *J. Mech. Phys. Solids*, 51(11):2259–2280, 2003.

[28] D. Choquet, D. P. Felsenfeld, and M. P. Sheetz. Extracellular matrix rigidity causes strengthening of integrin–cytoskeleton linkages. *Cell*, 88(1):39–48, 1997.

[29] I. Titushkin and M. Cho. Distinct membrane mechanical properties of human mesenchymal stem cells determined using laser optical tweezers. *Biophysical journal*, 90(7):2582–2591, 2006.

[30] E. M. Bonder, J. Colon, J. M. Dziedzic, and A. Ashkin. Force production by swimming sperm-analysis using optical tweezers. *J. Cell Biol*, 111:421a, 1990.

[31] M. P. MacDonald, G. C. Spalding, and K. Dholakia. Microfluidic sorting in an optical lattice. *Nature*, 426(6965):421–424, 2003.

[32] A. Pralle, M. Prummer, E. L. Florin, E. H. K. Stelzer, and J. K. H. Hörber. Three-dimensional high-resolution particle tracking for optical tweezers by forward scattered light. *Microscopy research and technique*, 44(5):378–386, 1999.

[33] K. Svoboda and S. M. Block. Biological applications of optical forces. *Annual review of biophysics and biomolecular structure*, 23(1):247–285, 1994.

[34] A. Ashkin. Optical trapping and manipulation of neutral particles using lasers. *Proceedings of the National Academy of Sciences*, 94(10):4853–4860, 1997.

[35] M. J. Lang and S. M. Block. Resource letter: Lbot-1: Laser-based optical tweezers. *American journal of physics*, 71(3):201, 2003.

[36] J. R. Moffitt, Y. R. Chemla, S. B. Smith, and C. Bustamante. Recent advances in optical tweezers. *Annu. Rev. Biochem.*, 77:205–228, 2008.

[37] A. Biebricher, W. Wende, C. Escudé, A. Pingoud, and P. Desbiolles. Tracking of single quantum dot labeled ecorv sliding along dna manipulated by double optical tweezers. *Biophysical journal*, 96(8):L50–L52, 2009.

[38] L. Ikin, D. M. Carberry, G. M. Gibson, M. J. Padgett, and M. J. Miles. Assembly and force measurement with spm-like probes in holographic optical tweezers. *New Journal of Physics*, 11(2):023012, 2009.

[39] Q. D. Pham, Y. Kusumi, S. Hasegawa, and Y. Hayasaki. Digital holographic microscope with low-frequency attenuation filter for position measurement of a nanoparticle. *Optics Letters*, 37(19):4119–4121, 2012.

[40] Y. F. Chen, G. A. Blab, and J. C. Meiners. Stretching submicron biomolecules with constant-force axial optical tweezers. *Biophysical journal*, 96(11):4701–4708, 2009.

[41] M. P. MacDonald, L. Paterson, K. Volke-Sepulveda, J. Arlt, W. Sibbett, and K. Dholakia. Creation and manipulation of three-dimensional optically trapped structures. *Science*, 296(5570):1101–1103, 2002.

[42] R. Phillips, J. Kondev, J. Theriot, H. Garcia, B. Chasan, et al. Physical biology of the cell. *American Journal of Physics*, 78:1230, 2010.

[43] P. A. Janmey and C. A. McCulloch. Cell mechanics: integrating cell responses to mechanical stimuli. *Annu. Rev. Biomed. Eng.*, 9:1–34, 2007.

[44] F. J. Alenghat and D. E. Ingber. Mechanotransduction: all signals point to cytoskeleton, matrix, and integrins. *Science Signaling*, 2002(119):pe6, 2002.

[45] K. S. Ko, P. D. Arora, and C. A. G. McCulloch. Cadherins mediate intercellular mechanical signaling in fibroblasts by activation of stretch-sensitive calcium-permeable channels. *Journal of Biological Chemistry*, 276(38):35967–35977, 2001.

[46] S. M. Block, L. S. B. Goldstein, and B. J. Schnapp. Bead movement by single kinesin molecules studied with optical tweezers. 1990.

[47] K. Svoboda and S. M. Block. Force and velocity measured for single kinesin molecules. *Cell*, 77(5):773–784, 1994.

[48] R. M. Simmonst, J. T. Finer, H. M. Warrick, B. Kralik, S. Chu, and J. A. Spudich. Force on single actin filaments in a motility assay measured with an optical trap. In *Mechanism of Myofilament Sliding in Muscle Contraction*, pages 331–337. Springer, 1993.

[49] P. Cluzel, A. Lebrun, C. Heller, R. Lavery, J. L. Viovy, D. Chatenay, and F. Caron. Dna: An extensible molecule. *Science*, 271(5250):792–794, 1996.

[50] S. B. Smith, L. Finzi, and C. Bustamante. Direct mechanical measurements of the elasticity of single dna molecules by using magnetic beads. *Science*, 258(5085):1122–1126, 1992.

[51] E. A. Abbondanzieri, W. J. Greenleaf, J. W. Shaevitz, R. Landick, and S. M. Block. Direct observation of base-pair stepping by rna polymerase. *Nature*, 438(7067):460–465, 2005.

[52] M. Grandbois, M. Beyer, M. Rief, H. Clausen-Schaumann, and H. E. Gaub. How strong is a covalent bond? *Science*, 283(5408):1727–1730, 1999.

[53] S. Hohng, R. Zhou, M. K. Nahas, J. Yu, K. Schulten, D. M. J. Lilley, and T. Ha. Fluorescence-force spectroscopy maps two-dimensional reaction landscape of the holliday junction. *Science*, 318(5848):279–283, 2007.

[54] S. R. Heidemann, S. Kaech, R. E. Buxbaum, and A. Matus. Direct observations of the mechanical behaviors of the cytoskeleton in living fibroblasts. *The Journal of cell biology*, 145(1):109–122, 1999.

[55] B. Daily, E. L. Elson, and G. I. Zahalak. Cell poking. determination of the elastic area compressibility modulus of the erythrocyte membrane. *Biophysical journal*, 45(4):671–682, 1984.

[56] M. Radmacher. Measuring the elastic properties of living cells by the atomic force microscope. *Methods in cell biology*, 68:67–90, 2002.

[57] R. M. Hochmuth. Micropipette aspiration of living cells. *Journal of biomechanics*, 33(1):15–22, 2000.

[58] N. Caille, O. Thoumine, Y. Tardy, and J. J. Meister. Contribution of the nucleus to the mechanical properties of endothelial cells. *Journal of biomechanics*, 35(2):177–187, 2002.

[59] A. R. Bausch, F. Ziemann, A. A. Boulbitch, K. Jacobson, and E. Sackmann. Local measurements of viscoelastic parameters of adherent cell surfaces by magnetic bead microrheometry. *Biophysical Journal*, 75(4):2038–2049, 1998.

[60] W. A. Ducker, T. J. Senden, and R. M. Pashley. Direct measurement of colloidal forces using an atomic force microscope. *nature*, 353(6341):239–241, 1991.

[61] D. Tabor and R. H. S. Winterton. Surface forces: Direct measurement of normal and retarded van der waals forces. *Nature*, 219:1120–1121, 1968.

[62] H. J. Butt, B. Cappella, and M. Kappl. Force measurements with the atomic force microscope: Technique, interpretation and applications. *Surface science reports*, 59(1):1–152, 2005.

[63] K. Svoboda and S. M. Block. Optical trapping of metallic rayleigh particles. *Optics letters*, 19(13):930–932, 1994.

[64] L. Novotny, R. X. Bian, and X. S. Xie. Theory of nanometric optical tweezers. *Physical Review Letters*, 79(4):645, 1997.

[65] J. C. Meiners and S. R. Quake. Direct measurement of hydrodynamic cross correlations between two particles in an external potential. *Physical review letters*, 82(10):2211, 1999.

[66] K. Nagayama, Y. Nagano, M. Sato, and T. Matsumoto. Effect of actin filament distribution on tensile properties of smooth muscle cells obtained from rat thoracic aortas. *Journal of biomechanics*, 39(2):293–301, 2006.

[67] R. E. Mahaffy, S. Park, E. Gerde, J. Käs, and C. K. Shih. Quantitative analysis of the viscoelastic properties of thin regions of fibroblasts using atomic force microscopy. *Biophysical journal*, 86(3):1777–1793, 2004.

[68] P. Fernández, P. A. Pullarkat, and A. Ott. A master relation defines the nonlinear viscoelasticity of single fibroblasts. *Biophysical journal*, 90(10):3796–3805, 2006.

[69] E. J. Koay, A. C. Shieh, and K. A. Athanasiou. Creep indentation of single cells. *Journal of biomechanical engineering*, 125(3):334–341, 2003.

[70] P. Roca-Cusachs, I. Almendros, R. Sunyer, N. Gavara, R. Farré, and D. Navajas. Rheology of passive and adhesion-activated neutrophils probed by atomic force microscopy. *Biophysical journal*, 91(9):3508–3518, 2006.

[71] C. W. J. Oomens, C. V. C. Bouten, D. L. Bader, and F. P. T. Baaijens. Viscoelastic properties of single attached cells under compression. *Journal of biomechanical engineering*, 127:237, 2005.

[72] V. M. Laurent, R. Fodil, P. Cañadas, S. Féréol, B. Louis, E. Planus, and D. Isabey. Partitioning of cortical and deep cytoskeleton responses from transient magnetic bead twisting. *Annals of biomedical engineering*, 31(10):1263–1278, 2003.

[73] R. Ananthakrishnan, J. Guck, F. Wottawah, S. Schinkinger, B. Lincoln, M. Romeyke, T. Moon, and J. Käs. Quantifying the contribution of actin networks to the elastic strength of fibroblasts. *Journal of theoretical biology*, 242(2):502–516, 2006.

[74] S. Park, D. Koch, R. Cardenas, J. Käs, and C. K. Shih. Cell motility and local viscoelasticity of fibroblasts. *Biophysical journal*, 89(6):4330–4342, 2005.

[75] J. S. H. Lee, P. Panorchan, C. M. Hale, S. B. Khatau, T. P. Kole, Y. Tseng, and D. Wirtz. Ballistic intracellular nanorheology reveals rock-hard cytoplasmic stiffening response to fluid flow. *Journal of cell science*, 119(9):1760–1768, 2006.

[76] N. Desprat, A. Richert, J. Simeon, and A. Asnacios. Creep function of a single living cell. *Biophysical journal*, 88(3):2224–2233, 2005.

[77] G. Binnig, C. F. Quate, and C. Gerber. Atomic force microscope. *Physical review letters*, 56(9):930, 1986.

[78] F. L. Leite and P. S. P. Herrmann. Application of atomic force spectroscopy (afs) to studies of adhesion phenomena: a review. *Journal of adhesion science and technology*, 19(3-5):365–405, 2005.

[79] H. Hertz. Über die berührung fester elastischer körper und über die härte. *J. für die reine u. angew. Math.*, 92, 1882.

[80] A. Ashkin. Acceleration and trapping of particles by radiation pressure. *Physical Review Letters*, 24(4):156–159, 1970.

[81] A. Ashkin. Forces of a single-beam gradient laser trap on a dielectric sphere in the ray optics regime. *Biophysical journal*, 61(2):569–582, 1992.

[82] M. J. Lang, C. L. Asbury, J. W. Shaevitz, and S. M. Block. An automated two-dimensional optical force clamp for single molecule studies. *Biophysical journal*, 83(1):491–501, 2002.

[83] K. C. Neuman, E. A. Abbondanzieri, R. Landick, J. Gelles, and S. M. Block. Ubiquitous transcriptional pausing is independent of rna polymerase backtracking. *Cell*, 115(4):437–447, 2003.

[84] M. Speidel, L. Friedrich, and A. Rohrbach. Interferometric 3d tracking of several particles in a scanning laser focus. *Optics express*, 17(2):1003–1015, 2009.

[85] A. Kusumi, Y. Sako, and M. Yamamoto. Confined lateral diffusion of membrane receptors as studied by single particle tracking (nanovid microscopy).

effects of calcium-induced differentiation in cultured epithelial cells. *Biophysical journal*, 65(5):2021–2040, 1993.

[86] J. P. Shelby, J. S. Edgar, and D. T. Chiu. Monitoring cell survival after extraction of a single subcellular organelle using optical trapping and pulsed-nitrogen laser ablation. *Photochemistry and photobiology*, 81(4):994–1001, 2004.

[87] S. Maeda, T. Sugiura, and K. Minato. Optical tweezers with assistance of sub-microsecond-duration pulse laser beam. *Applied Physics Express*, 5(4):2701, 2012.

[88] D. P. Felsenfeld, P. L. Schwartzberg, A. Venegas, R. Tse, and M. P. Sheetz. Selective regulation of integrin–cytoskeleton interactions by the tyrosine kinase src. *Nature Cell Biology*, 1(4):200–206, 1999.

[89] T. Sugiura, H. Miyoshi, T. Nishio, and A. Honda. Cell palpation with an optically trapped particle. *Journal of Micro-Nano Mechatronics*, 7(4):131–136, 2012.

[90] M. Padgett, J. Molloy, and D. McGloin. Optical tweezers: Methods and applications, series in optics and optoelectronics. *Taylor and Francis Group*, 2010.

[91] E. Fällman and O. Axner. Design for fully steerable dual-trap optical tweezers. *Applied Optics*, 36(10):2107–2113, 1997.

[92] JPK Instruments Product overview. Nanotracker 2 ™, July 2013.

[93] M. Zhong, J. Zhou, J. Wu, and Y. Li. Determination of the axial stiffness of an optical trap with information entropy signals. In *Proc. of SPIE Vol*, volume 7507, pages 75070J–1, 2009.

[94] T. Ota, S. Kawata, T. Sugiura, M. J. Booth, M. A. A. Neil, R. Juškaitis, and T. Wilson. Dynamic axial-position control of a laser-trapped particle by wave-front modification. *Optics letters*, 28(6):465–467, 2003.

[95] Y. Huang, J. Wan, M. C. Cheng, Z. Zhang, S. M. Jhiang, and C. H. Menq. Three-axis rapid steering of optically propelled micro/nanoparticles. *Review of Scientific Instruments*, 80(6):063107–063107, 2009.

[96] L. Zhu, P. C. Sun, D. U. Bartsch, W. R. Freeman, and Y. Fainman. Wavefront generation of zernike polynomial modes with a micromachined membrane deformable mirror. *Applied optics*, 38(28):6019–6026, 1999.

[97] D. Malacara and S. L. DeVore. Interferogram evaluation and wavefront fitting. *Optical shop testing*, 2, 1992.

[98] E. Theofanidou, L. Wilson, W. J. Hossack, and J. Arlt. Spherical aberration correction for optical tweezers. *Optics communications*, 236(1):145–150, 2004.

[99] J. Liesener, M. Reicherter, T. Haist, and H. J. Tiziani. Multi-functional optical tweezers using computer-generated holograms. *Optics Communications*, 185(1):77–82, 2000.

[100] T. Higuchi, Q. D. Pham, S. Hasegawa, and Y. Hayasaki. Three-dimensional positioning of optically trapped nanoparticles. *Applied Optics*, 50(34):H183–H188, 2011.

[101] A. Rohrbach. Stiffness of optical traps: quantitative agreement between experiment and electromagnetic theory. *Physical review letters*, 95(16):168102, 2005.

[102] K. C. Neuman and S. M. Block. Optical trapping. *Review of scientific instruments*, 75(9):2787–2809, 2004.

[103] K. Berg-Sørensen and H. Flyvbjerg. Power spectrum analysis for optical tweezers. *Review of Scientific Instruments*, 75(3):594–612, 2004.

[104] E. J. G. Peterman, F. Gittes, and C. F. Schmidt. Laser-induced heating in optical traps. *Biophysical journal*, 84(2):1308–1316, 2003.

[105] N. Malagnino, G. Pesce, A. Sasso, and E. Arimondo. Measurements of trapping efficiency and stiffness in optical tweezers. *Optics communications*, 214(1-6):15–24, 2002.

[106] M. S. Rocha. Optical tweezers for undergraduates: theoretical analysis and experiments. *American Journal of Physics*, 77:704, 2009.

[107] S. Henon, G. Lenormand, A. Richert, and F. Gallet. A new determination of the shear modulus of the human erythrocyte membrane using optical tweezers. *Biophysical Journal*, 76(2):1145–1151, 1999.

[108] K. H. Parker and C. P. Winlove. The deformation of spherical vesicles with permeable, constant-area membranes: application to the red blood cell. *Biophysical journal*, 77(6):3096–3107, 1999.

[109] B. Schnurr, F. Gittes, F. C. MacKintosh, and C. F. Schmidt. Determining microscopic viscoelasticity in flexible and semiflexible polymer networks from thermal fluctuations. *Macromolecules*, 30(25):7781–7792, 1997.

[110] A. J. Levine and T. C. Lubensky. Two-point microrheology and the electrostatic analogy. *Physical Review E*, 65(1):011501, 2001.

[111] E. Evans and A. Yeung. Apparent viscosity and cortical tension of blood granulocytes determined by micropipet aspiration. *Biophysical Journal*, 56(1):151–160, 1989.

[112] L. D. Landau and E. M. Lifshitz. Theory of elasticity, 1970.

[113] L. R. G. Treloar. *The physics of rubber elasticity*. Oxford University Press, 1975.

[114] E. Dintwa, E. Tijskens, and H. Ramon. On the accuracy of the hertz model to describe the normal contact of soft elastic spheres. *Granular Matter*, 10(3):209–221, 2008.

[115] M. Rahmat, H. Ghiasi, and P. Hubert. An interaction stress analysis of nanoscale elastic asperity contacts. *Nanoscale*, 4(1):157–166, 2012.

[116] C. A. Putman, K. O. van der Werf, B. G. de Grooth, N. F. Van Hulst, and J. Greve. Viscoelasticity of living cells allows high resolution imaging by tapping mode atomic force microscopy. *Biophysical journal*, 67(4):1749–1753, 1994.

[117] R. E. Mahaffy, C. K. Shih, F. C. MacKintosh, and J. Käs. Scanning probe-based frequency-dependent microrheology of polymer gels and biological cells. *Physical Review Letters*, 85(4):880, 2000.

[118] O. Otto, F. Czerwinski, J. L. Gornall, G. Stober, L. B. Oddershede, R. Seidel, and U. F. Keyser. Real-time particle tracking at 10,000 fps using optical fiber illumination. *Opt. Express*, 18(22):22722–22733, 2010.

[119] S. Keen, J. Leach, G. Gibson, and M. J. Padgett. Comparison of a high-speed camera and a quadrant detector for measuring displacements in optical tweezers. *Journal of Optics A: Pure and Applied Optics*, 9(8):S264, 2007.

[120] C. Veigel, M. L. Bartoo, D. White, J. C. Sparrow, and J. E. Molloy. The stiffness of rabbit skeletal actomyosin cross-bridges determined with an optical tweezers transducer. *Biophysical journal*, 75(3):1424–1438, 1998.

[121] Z. Li, B. Anvari, M. Takashima, P. Brecht, J. H. Torres, and W. E. Brownell. Membrane tether formation from outer hair cells with optical tweezers. *Biophysical journal*, 82(3):1386–1395, 2002.

[122] Y. Shitamichi, M. Ichikawa, and Y. Kimura. Mechanical properties of a giant liposome studied using optical tweezers. *Chemical Physics Letters*, 479(4-6):274–278, 2009.

[123] A. van der Horst, N. R. Forde, et al. Calibration of dynamic holographic optical tweezers for force measurements on biomaterials. *Optics express*, 16(25):20987–21003, 2008.

[124] M. C. Dy. Integration of Axial Displacement in Optical Tweezers. Master's thesis, Nara Institute of Science and Technology, Nara, Japan, 2011.

[125] M. Radmacher. Studying the mechanics of cellular processes by atomic force microscopy. *Methods in cell biology*, 83:347–372, 2007.

[126] A. Touhami, B. Nysten, and Y. F. Dufrêne. Nanoscale mapping of the elasticity of microbial cells by atomic force microscopy. *Langmuir*, 19(11):4539–4543, 2003.

[127] G. Lenormand, S. Hénon, A. Richert, J. Siméon, and F. Gallet. Direct measurement of the area expansion and shear moduli of the human red blood cell membrane skeleton. *Biophysical journal*, 81(1):43–56, 2001.

[128] E. A-Hassan, W. F. Heinz, M. D. Antonik, N. P. D'Costa, S. Nageswaran, C.A. Schoenenberger, and J. H. Hoh. Relative microelastic mapping of living cells by atomic force microscopy. *Biophysical Journal*, 74(3):1564–1578, 1998.

Appendix

This appendix covers the programs utilized in translating the lens L1 and image analysis. In the image analysis program, the inspection procedures will be discussed based on how the analysis is done in the experiments. The lens L1 program is created using LabVIEW program, while the image analysis is created using NI Vision Builder for Automated Inspection.

A User Interface

A.1 Len L1 Controller

- Main menu of the lens L1 controller program is illustrated in Fig. A.1.

  The image taken by the CCD camera is shown in real time in the **Image** window. On the left side of the image window, users can choose from several commands, such as magnify, and create shapes, and use the chosen command to manipulate the image window (not the actual image itself). **Wait time** denotes how many milliseconds the lens L1 will move after each step. The position of the lens L1 is shown in the **Current Pos** display. Each functions of the buttons will be discussed in the next items.

- Click the **play** button under the menu bar.

  The play button starts the program. The real-time image will begin showing in the image window.

- Set the **number of steps** the lens L1 will be translated. Place a **negative** sign to specify downward movement.

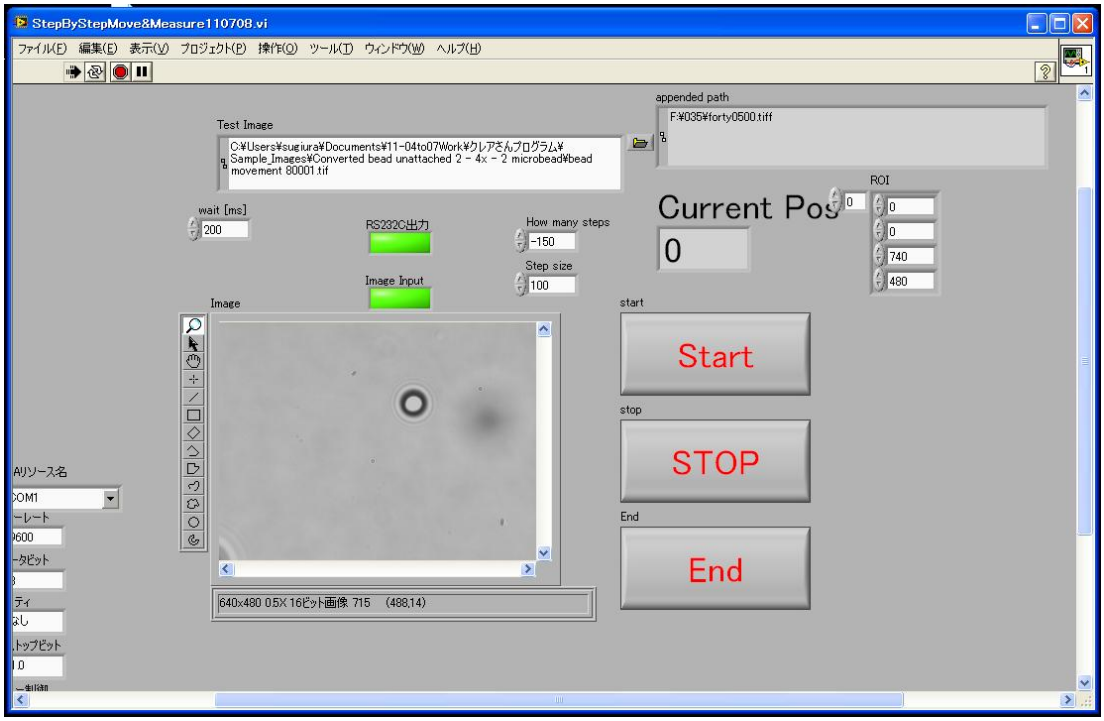

Figure A.1: Lens L1 translation controller program

A positive (no negative sign) number of steps denotes translating the lens L1 closer to the microscope, while placing a negative sign specifies the lens L1 to move away from the microscope.

- Specify the **step size**. That is, how long the lens L1 will move per step. The step size is set in unit micrometer. In the experiments, the step size is set to 100.

- Click the **Start** button to begin the process of capturing the image and translating the lens L1.

  Before the actual process, a pop up menu appears. The pop up menu asks the user at which directory the images will be saved.

- The process will stop until the lens L1 reached the specified number of steps. Afterwards, the lens L1 will be translated back to the initial position.

- Click the **STOP** button to discontinue the process in progress.

  This button does not terminate the running program. Rather, this only stops capturing and saving the images. At the instance this button is clicked, the lens L1 is translated back to the initial position.

- The **End** button terminates the entire program. The **Stop** button under the menu bar also has the same function.

  Clicking this button terminates the entire program. If clicked during the process, capturing the image will halt, and the lens L1 will not return to the initial position.

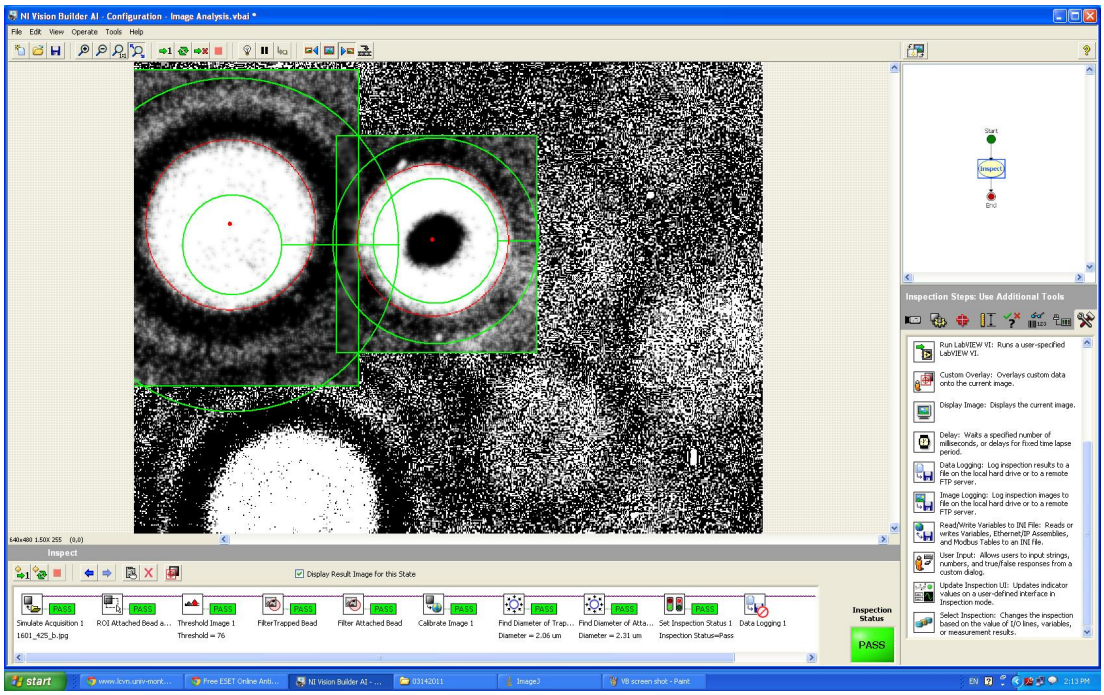

Figure A.2: Image analysis program

A.2 Image Analysis

- Main menu of the lens L1 controller program is illustrated in Fig. A.2).

  The menu bar and buttons under the menu bar are self-explanatory. The image window shows the particular image file. The Inspect window below the image window can be modified by the user to include the necessary steps to acquire the particle size. In Fig. A.2, the different steps are chosen to inspect two particles. Vision Builder reads files with .tif file extension.

- Start the process by clicking the run button.

- In the Simulate Acquisition step, load the chosen calibration image, that is, the particle image taken at the initial lens L1 position is acquired.

  This step is necessary so that the output text file will include the apparent diameter measurement of the particle in unit micrometers, and not just in pixel values.

- The image will be enclosed in the Region of Interest (ROI).

  The image processing will only be applied within the ROI.

- The threshold is adjusted to highlight the particle image.

- Filter is applied to reject the noise.

- Calibration process is performed. At this step, a pop out menu appears. Complete the steps in order to convert the pixel values into real-world units.

- The Find Diameter step calculates the diameter of the particle image.

  This step is actually the Find Circular Edge detector. The process is discussed in Section 3.2.5.

- Data logging step outputs the apparent particle diameter and other information as a text file.

- Start the inspection process for the raw data.

  The user can choose to analyse a single image file from a given folder, or continuously analyse all the images from a given folder.

  Since the Calibrate image step is already set, the calibrate step will simply convert all the pixel diameter values into the specified real-world unit.